CERN/SPSC 2000–032
SPSC/P284 Add. 2
17 August 2000

First Observation of πK Atom and its Lifetime Measurement

B. Adeva[p], L. Afanasyev[l], Z. Berka[b], V. Brekhovskikh[o], G. Caragheorgheopol[m], T. Cechak[b], M. Chiba[j], S. Costantini[q], S. Constantinescu[m], C.C. Detraz[a], A. Doudarev[l], D. Drijard[a], I. Evangelou[d], M. Ferro-Luzzi, M.V. Gallas[a,p], J. Gerndt[b], R. Giacomich[f], P. Gianotti[e], M. Giardoni[e], D. Goldin[q], F. Gomez[p], A. Gorin[o], O. Gortchakov[l], C. Guaraldo[e], M. Hansroul[a], R. Hosek[b], M. Iliescu[e,m], M. Jabitski[l], N. Kalinina[n], V. Karpoukhine[l], J. Kluson[b], M. Kobayashi[g], P. Kokkas[d,q], V. Komarov[l], A. Koulikov[l], A. Kouptsov[l], V. Krouglov[l], L. Krouglova[l], K.-I. Kuroda[k], A. Lamberto[f], A. Lanaro[a,e], V. Lapshin[o], R. Lednicky[c], P. Levi Sandri[e], A. Lopez Aguera[p], V. Lucherini[e], T. Maki[i], I. Manuilov[o], N. Manthos[d], M. Medinsky[o], L. Montanet[a], L. Nemenov[a,l], M. Nikitin[l], K. Okada[h], V. Olchevskii[l], M. Pentia[m], A. Penzo[f], C. Petrascu[e,m], M. Plo[p], T. Ponta[m], D. Pop[m], Zh. Pustylnik[l], G.F. Rappazzo[f], A. Riazantsev[o], X.M. Rodriguez[p], A. Rodriguez Fernandez[p], V. Rykalin[o], C. Santamarina[p], J. Saborido[p], J. Schacher[r], C. Schuetz[q], A. Sidorov[o], J. Smolik[c], F. Takeutchi[h], A. Tarasov[l], L. Tauscher[q], M.J. Tobar[p], F. Triantis[d], S. Trousov[n], S. Vlachos[q], V. Yazkov[n], Y. Yoshimura[g], P. Zrelov[l]

[a] CERN, Geneva, Switzerland
[b] Czech Technical University, Prague, Czech Republic
[c] Institute of Physics ASCR, Prague, Czech Republic
[d] University of Ioannina, Greece
[e] INFN - Laboratori Nazionali di Frascati, Frascati, Italy
[f] Trieste University and INFN-Trieste, Italy
[g] KEK, Tsukuba, Japan
[h] Kyoto Sangyo University, Japan
[i] UOEH-Kyushu, Japan
[j] Tokyo Metropolitan University, Japan
[k] Waseda University, Japan
[l] JINR Dubna, Russia
[m] National Institute for Physics and Nuclear Engineering IFIN-HH, Bucharest, Romania
[n] Skobeltsyn Institute for Nuclear Physics of Moscow State University Moscow, Russia
[o] IHEP Protvino, Russia
[p] Santiago de Compostela University, Spain
[q] Basel University, Switzerland
[r] Bern University, Switzerland

GENEVA
2000

Contents

Introduction

Scattering amplitudes of the $\pi\pi$ and πK system at low energies are usually expressed in terms of scattering lengths. To evaluate the scattering lengths in the framework of QCD effective Lagrangians or lattice calculations may be used. An effective Lagrangian can be constructed using the chiral symmetry breaking mechanism and other well established symmetries. The effective Lagrangian of Chiral Perturbation Theory (ChPT) allows to calculate S-wave $\pi\pi$ and πK scattering lengths with $\sim 3\%$ and $\sim 10\%$ accuracy, respectively. For the $\pi\pi$ system these calculations have not yet been tested at this level of accuracy, but different experiments (DIRAC at CERN, E865 at Brookhaven, KLOE at DAΦNE) are attempting to measure $\pi\pi$ scattering lengths with a precision of $\sim 5\%$. For πK scattering lengths, model independent data are not available, but a clean way to achieve this goal would be to measure the lifetime τ of hydrogen-like atoms formed by π^+ and K^- ($A_{\pi K}$) or by K^+ and π^- ($A_{K\pi}$). In fact, there exists a precise relationship between the decay probability of the atom in the ground state into $\pi^0\overline{K^0}$ and the S-wave πK scattering lengths, valid at leading order in isospin breaking:

$$W(A_{\pi^+K^-} \to \pi^0\overline{K^0}) = C(a_{1/2} - a_{3/2})^2 \tag{1}$$

where $a_{1/2}$ and $a_{3/2}$ are the scattering lengths for the isospin 1/2 and 3/2 states, and C is known at leading order in isospin breaking. Because the decay channel in eq. (1) is by far the dominant one, CHPT can predict a value for τ by taking into account only this *strong* decay: $\tau \approx 5 \cdot 10^{-15}$ s.

In the $\pi\pi$ case, a precise measurement of scattering lengths provides a crucial test for the modern concept of chiral symmetry breaking in processes, where only u and d quarks are involved. On the other hand, a measurement of πK scattering lengths will extend this test to processes including the s quark as well.

In order to produce the atoms $A_{\pi^+K^-}$ and $A_{K^+\pi^-}$ and measure their lifetime, we plan to use the PS proton beam and the DIRAC setup, presently taking data to measure the $\pi^+\pi^-$ atom ($A_{2\pi}$) lifetime. Step-by-step the setup has to be modified in order to achieve optimal conditions for detecting πK pairs from $A_{\pi K}$ ionisation without affecting the $\pi^+\pi^-$ data taking.

The following strategy is foreseen:

First step: Detection of $A_{\pi^+K^-}$ and $A_{K^+\pi^-}$, by using the present symmetric setup geometry, simply upgraded with a new set of threshold Cherenkov counters and with an additional (third) scintillating fibre plane. These new Cherenkov counters will not affect the measurements on $A_{2\pi}$, whereas they will allow to detect in the same setup, simultaneously, also π^+K^- and π^-K^+ pairs from $A_{\pi^+K^-}$ and $A_{K^+\pi^-}$ ionisation in the target, respectively. This first step will be crucial, since it will allow to verify:

a) the feasibility of $A_{\pi K}$ detection and lifetime measurement with the same method as in the case of $A_{2\pi}$;

b) the yield of π^+K^- pairs from "ionised atoms" in the DIRAC setup;
c) the possibility to detect $A_{K^+\pi^-}$, since K^+ are heavily contaminated by proton background. This is a relevant point, since the lifetime of both atoms are equal, and a dedicated Monte Carlo calculation of p–nucleus interaction predicts an almost twice larger yield of $A_{K^+\pi^-}$ with respect to that of $A_{\pi^+K^-}$. Hence the gain in statistics is obvious if also $A_{K^+\pi^-}$ can be detected.

Moreover, since this upgrade does not affect the ordinary $A_{2\pi}$ data taking, it can be implemented in shorter time compared to a dedicated study of $A_{\pi K}$. The step-by-step upgrade allows to introduce new Cherenkov detectors during the shut-down period at the end of 2001 and to obtain the required information on $A_{\pi K}$ at the end of 2002, while completing the collection of $A_{2\pi}$ data.
Second step: According to the results of data taking during the first upgrade, a dedicated setup geometry for $A_{\pi K}$ detection can be envisaged. Since the pion and kaon from $A_{\pi K}$ breakup have momenta differing by a factor 3.5, an asymmetric setup geometry for the two arms spectrometer is mandatory in order to optimise the detection of such pairs. An asymmetric setup will, however, not allow the simultaneous detection of $A_{\pi^+K^-}$ and $A_{K^+\pi^-}$. According to the results of "first upgrade" measurements a choice should be made. If the separation of K^+ from p proves to be insufficient, the $A_{\pi^+K^-}$ configuration, free from proton background, should be selected. If on the other hand the K^+/p separation is successful, the configuration with the two times higher yield for $A_{K^+\pi^-}$ will be selected. It is worthwhile to note that, the $A_{2\pi}$ yield in the asymmetric configuration (optimised for $A_{\pi K}$ detection), will still not be negligible.

To summarise the second-step upgrade, to be started in 2003, the following action are foreseen:

- rotation of the secondary channel by an angle of -1.5° (in the median setup plane).
- rotation of the downstream detectors in the same plane by $+4^\circ$.
- final installation of Cherenkov counters.
- a further (forth) scintillating fibre plane.
- upgrading variants for the upstream (of the magnet) tracking device:
  - new triple GEM detector (Gas Electron Multiplier) to replace the present MSGC (MicroStrip Gas Chamber) with 1 GEM.
  - installation of a dedicated small size drift chamber.
  - installation of a double-sided silicon microstrip detector.
  - combination of the above variants.
- a faster (100 Mbit/s) Ethernet connection among the DAQ computers and between DAQ host computer and central recorder, to manage the increased trigger rate foreseen.

The second step of upgrade should be done in 2003, and data could be taken in 2004 and 2005.

Chapter 1

Theoretical motivation

1.1 Chiral Symmetry, Chiral Perturbation Theory and $\pi\pi$ scattering

The theory of strong interaction within the framework of standard model, Quantum ChromoDynamics (QCD), exhibits two distinct features: asymptotic freedom and colour confinement. At large momentum transfer, the QCD predictions have successfully been tested in many reactions, but these results cover only one aspect of the theory, namely the asymptotic freedom. It is also of great importance to study the non-perturbative region of QCD in order to fully understand the dynamics of strongly interacting hadrons.

Let us consider QCD with only two flavours: u and d. With the hypothesis of massless quarks, $\mathcal{L}_{QCD}$ is invariant under chiral $SU(2)_L \times SU(2)_R$ transformations. On the other hand, the observed hadron spectrum suggests that the ground state of the theory (QCD vacuum) is asymmetric under the action of this group (spontaneous breakdown of the chiral symmetry). As a consequence of this asymmetry, three massless pseudo-scalar particles (Goldstone bosons) must appear in the spectrum. The three lightest hadrons, $\pi^{\pm}$ and π^0, are indeed pseudoscalars, but not exactly massless as appropriate for Goldstone bosons. To get a mass for the real pions, it is necessary to break the chiral symmetry $SU(2)_L \times SU(2)_R$ of $\mathcal{L}_{QCD}$ by introducing u and d quarks with masses m_u and m_d, respectively. The Goldstone nature of the pseudoscalar mesons, weakly interacting at low energy, allows to study their mutual interactions within the framework of an effective theory, which is formulated in terms of physical fields [WEIN68, WEIN79, LEUT93] instead of quark and gluon degrees of freedom. The structure of this effective Lagrangian is determined by Lorentz invariance, P-, C-invariance and by the *chiral symmetry*. At low energy the elements of the S-matrix can be evaluated using Chiral Perturbation Theory (ChPT) [WEIN79, GASS83, LEUT93, LEUT94, CHPT]. ChPT is mathematically equivalent to QCD [WEIN79, LEUT93], but the effective Lagrangian is constructed as an expansion in powers of the external momenta and of the quark masses:

$$\mathcal{L}_{eff} \equiv \mathcal{L}_{(2)} + \mathcal{L}_{(4)} + \mathcal{L}_{(6)} + ... \tag{1.1}$$

where the indices denote the number of derivatives (powers of external momenta) and quark mass insertions. Within the framework of ChPT, the elastic $\pi\pi$ scattering amplitude is also expressed by an expansion in powers of the external momenta p and of the

light quark masses:

$$A = A_2 + A_4 + A_6 + \cdots \tag{1.2}$$

where A_n is of the order $O(p^n)$. The leading-order term A_2 has been calculated by Weinberg [WEIN66] and the next-to-leading order term A_4 by Gasser and Leutwyler [GASS83]. The calculation of A_6 [BIJN96, BIJN97] has been carried out as well (see also ref. [KNEC95]). Very recently, the values of the S-wave pion-pion scattering lengths with isospin 0 and 2 were determined with high precision better than 3% [COLA00]:

$$a_0 = 0.220 \pm 0.005; \quad a_2 = -0.0444 \pm 0.0010; \quad a_0 - a_2 = 0.265 \pm 0.004. \tag{1.3}$$

Here the scattering lengths are given in units of $M_{\pi^+}^{-1}$.

1.2 Quark condensate and $\pi\pi$ scattering

Many years ago it has been assumed [GELL68, GLAS68] that the spontaneous breaking of chiral symmetry is due to a strong condensation of quark-antiquark pairs in vacuum. The quark condensate parameter in the $SU(2)_L \times SU(2)_R$ case

$$B = -\lim_{m_q \to 0} \frac{1}{F_\pi^2} \langle 0|\bar{q}q|0\rangle, \quad q = (u, d), \tag{1.4}$$

is then considered to play a dominant role in the description of the symmetry-breaking effects. The analogue of this relation in the $SU(3)_L \times SU(3)_R$ ChPT reads as

$$B_0 = -\lim_{m_q \to 0} \frac{1}{F_\pi^2} \langle 0|\bar{q}q|0\rangle, \quad q = (u, d, s). \tag{1.5}$$

A scenario alternative to the standard case — with a weak quark condensation — was also considered [FUCH91, STER93, KNEC95, SAZD00]. In a recent paper [DESC00] the influence of the vacuum fluctuations of $\bar{q}q$ pairs on low-energy constants and condensates was studied.

The assumption of a strong quark condensation together with its consequences has not been tested experimentally so far. The $\pi\pi$ scattering at low energy is a promising ground for studying the strength of the quark condensate. The predictions for the $\pi\pi$ scattering lengths given in eq.1.3 are based on the standard scenario of symmetry breaking (large condensate) in the $SU(2)_L \times SU(2)_R$ ChPT. Therefore, any substantial deviation of the measured values of the scattering lengths from the ones given in (1.3) would signal the breakdown of the standard scenario.

1.3 Lattice Calculations

ChPT exploits only one part of the information contained in the Lagrangian of QCD, its symmetry properties. Lattice calculations can do more: they allow, in principle, to evaluate the full set of Green functions at any momentum value in terms of the scale of the theory and of the quark masses. In particular, it is possible, in principle, to calculate the unknown low-energy constants which occur in the effective Lagrangian. Unfortunately, this program has not yet reached the accuracy reached by ChPT. At present, a_0 and a_2 have been determined with an accuracy of $\sim 10\%$ [FUKU95, AOKI99].

1.4 Chiral Symmetry, Chiral Perturbation Theory and πK scattering

The QCD Lagrangian with three flavours u, d and s in the case of massless quark is invariant under chiral $SU(3)_L \times SU(3)_R$ transformations. The 8 pseudo-scalar hadrons π, K and η with their masses suggest that:

— QCD vacuum is asymmetric under the action of this group;

— The masses of u, d and s quarks differ from zero and for this reason the QCD Lagrangian is non-invariant under chiral $SU(3)_L \times SU(3)_R$ transformations.

As in the case of pions, the interaction of pions and kaons can be studied using an effective Lagrangian, whose structure is determined by Lorentz invariance, P-, C-invariance and by *chiral* $SU(3)_L \times SU(3)_R$ *symmetry*. The Goldstone nature of pseudo-scalar mesons imply that their interaction at low energy is weak and that they can be studied in the framework of ChPT. In ChPT, the effective Lagrangian and the elastic πK scattering amplitude may be expressed as an expansion in powers of the external momenta p and of u, d and s quark masses:

$$\mathcal{L}_{eff} = \mathcal{L}_{(2)} + \mathcal{L}_{(4)} + \mathcal{L}_{(6)} + \cdots \tag{1.6}$$

$$A = A_2 + A_4 + A_6 + \cdots \tag{1.7}$$

where $\mathcal{L}_{(n)}$ and A_n are of the order of $O(p^n)$. Since the mass of the s quark is greater than those of the u and d quarks, the convergence of eq. (1.7) is expected to be slower than in the case of $\pi\pi$ scattering amplitude. In this framework, one foresees that the precision of the calculation of the πK scattering lengths is smaller than that of the $\pi\pi$ scattering lengths for the same order of ChPT calculations. For an alternative method of calculation, where the expansion is done at a fixed physical value for m_s, we refer to ref. [ROES99].

The study of πK scattering would test our understanding of chiral $SU(3)_L \times SU(3)_R$ symmetry breaking of QCD while the investigation of $\pi\pi$ scattering allows us to perform the same check on $SU(2)_L \times SU(2)_R$ symmetry breaking. This is the main difference between $\pi\pi$ and πK scattering investigations.

The leading contribution in (1.1) and (1.6) is indeed the sum of the chiral invariant term $\mathcal{L}_{(2)}^{inv}$ and of the symmetry breaking term $\mathcal{L}_{(2)}^{noninv}$ (mass term). In the isospin symmetric case ($m_u = m_d$), the $\pi\pi$ scattering amplitude has contributions from both $\mathcal{L}_{(2)}^{inv}$ and $\mathcal{L}_{(2)}^{noninv}$ while the πK scattering amplitude depends only form $\mathcal{L}_{(2)}^{inv}$. On the other hand, if isospin symmetry is broken ($m_u \neq m_d$) the $\pi\pi$ amplitude is insensitive to this effect even at order $O(p^4)$, while the πK amplitude ($\pi K \to \pi^0 K^0$) contains a term $B_0(m_d - m_u)$ already at order p^2. This is one of the few cases, where the quark mass difference $m_d - m_u$ affects a scattering amplitude already at leading order.

The πK scattering amplitude has been evaluated at next-to-leading order using ChPT [BERN91]. The leading amplitude A_2 may be obtained from the tree graph of fig. 1.1*a*. The next-to-leading order contribution A_4 is due to the one-loop diagrams generated by $\mathcal{L}_{(2)}$ (fig. 1.1*c*,*d*) and to the tree graph from $\mathcal{L}_{(4)}$ (fig. 1.1*b*).

For the S-wave πK scattering lengths with isospin 1/2 and 3/2 the following values in units of $M_{\pi^+}^{-1}$ have been predicted [BERN91]:

$$a_{1/2} = 0.19 \pm 0.02; \qquad a_{3/2} = -0.05 \pm 0.02. \tag{1.8}$$

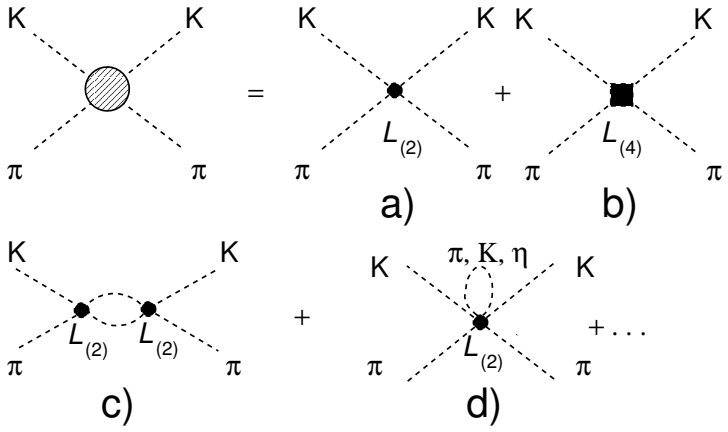

Figure 1.1: *The πK scattering amplitude in the one loop approximation. The diagrams a) and b) display the contribution of $\mathcal{L}_{(2)}$ and $\mathcal{L}_{(4)}$. The graphs c) and d) show one-loop corrections.*

The errors in (1.8) are due to the uncertainties of the low energy constants and to higher order corrections ($\mathcal{L}_{(6)}$ and two-loops). By means of the alternative method mentioned above, a recent calculation [ROES99] lead to a precise value of

$$a_{1/2} - a_{3/2} = 0.23 \pm 0.01, \tag{1.9}$$

in good agreement with the previous ones.

1.5 Quark condensate and πK scattering

If the $SU(3)_L \times SU(3)_R$ quark condensate, in the chiral limit, is large $\langle 0|\bar{q}q|0\rangle \approx (-222 \text{ MeV})^3$, then it follows for the ratio

$$\frac{m_s}{\hat{m}} = \frac{2M_K^2}{M_\pi^2} - 1 + \textit{small corrections} \approx 26 \tag{1.10}$$

where $\hat{m} = (m_u + m_d)/2$, and m_s is the mass of the s quark. But if the quark condensate is small [FUCH91, STER93, KNEC95], then $r = m_s/\hat{m}$ as a free parameter depends on the value of the condensate itself, and can take any value in the interval

$$6.3 \leq \frac{m_s}{\hat{m}} \leq 26, \tag{1.11}$$

The value of the quantity $(a_{1/2} - a_{3/2})$ may be determined in a measurement of the $A_{\pi K}$ atom lifetime. However, this quantity at leading order and hence the $A_{\pi K}$ lifetime do not depend on $r = m_s/\hat{m}$. On the other hand, the quantity $(2a_{3/2} + a_{1/2})$ which goes to zero if $m_s/\hat{m} \approx 26$ at leading order in ChPT, is sensitive to the deviation of r from the result in eq. (1.10) [KNEC93]. This combination between $a_{1/2}$ and $b_{3/2}$ can be obtained, in principle, by a measurement of the energy difference between 2S and 2P atomic levels, because the strong part of this energy difference is proportional to $(2a_{3/2} + a_{1/2})$.

1.6 πK scattering: experimental results

In the 60's and 70's several experiments were performed to measure πK scattering lengths. Most of them were done studying the scattering of kaons off protons or neutrons, and later also off deuterons. The kaon beams used in these experiments had energies ranging from 2 to 13 GeV.

The main idea of those experiments was to determine the contribution of the One Pion Exchange (OPE) mechanism. This allows to obtain the πK scattering amplitude. Due to kinematical restrictions it is not possible to have an on mass shell propagated pion ($t \neq M_\pi^2$, $t < 0$). Therefore, one has to determine the scattering amplitude for $t < 0$, and then extrapolate the results to $t = M_\pi^2$.

Some of the processes studied are listed below:

$K^+p \to$	$K^+\pi^-\Delta^{++}$	[TRIP68, MERC71, BING72, MATI74]
	$K^0\pi^0\Delta^{++}$	[CHLI75, DUNW77, BRAN77, ESTA78]
	$K^+\pi^+\Delta^0$	[DEBA69]
	$K^0\pi^+p$	[BAKE75, BALD76, BALD78, MART78]
	$K^+\pi^+n$	[DUNW77, ESTA78, BRAN77]
$K^-p \to$	$K^-\pi^-\Delta^{++}$	[KIRS71, JONG73, LING73, BRAN77, DUNW77, ESTA78]
	$K^-\pi^+n$	[YUTA71, AGUI73, FOX74, LAUS75, GRAE77, SPIR77, DUNW77, BRAN77, ESTA78]
	$K^-\pi^0p$	[AGUI73, GRAE77, SPIR77]
	$\overline{K}^0\pi^-p$	[AGUI73, GRAE77, SPIR77, BALD78, MART78]
$K^+n \to$	$K^+\pi^-p$	[FIRE72, FOX74, BAKE75]
	$K^0\pi^+n$	[BAKE75]
$K^-n \to$	$K^-\pi^+p$	[BAKK70, CHO70, ANTI71]

Three methods were used for this extrapolation:

— direct extrapolation of the measured cross-section into the mass shell region [MATI74];

— decomposition of the measured cross-section into spherical functions and their extrapolation into the mass shell region [BING72];

— consideration of all the production processes in the amplitude analysis (not only OPE) and then extrapolation to the mass shell region [FOX74, BAKE75, ESTA78].

In the first method, a theoretical cross-section σ_{th} is constructed, then the ratio $\widehat{\sigma} = \sigma_{exp}/\sigma_{th}$ is extrapolated to $t = M_\pi^2$. The final result depends strongly on the parametrisation chosen for σ_{th}. Moreover, this method doesn't allow one to combine data from different experiments.

The second method avoids some limitations of the first one. One combines data from different experiments, but encounters problems with singular behaviour around $t = 0$. These problems can lead to incorrect results.

The third method, widely used in later works, is a more complex one. It allows to combine the results from all the experiments, but this approach is still model dependent. If one takes into account only S and P waves in πK scattering, eight complex helicity

amplitudes are needed to construct the global amplitude. Furthermore, only six independent quantities can be extracted from the experimental data. Therefore, some parameters must be fixed using a strong interaction model.

For a more detailed descriptions of these methods we refer to ref. [LANG78].

Table 1.1: *Measured πK S-wave scattering lengths for the isospin $I = 1/2$ state.*

reference	[BING72]	[MATI74]	[FOX74]	[ESTA78]
$a_{1/2}$	0.168	0.220 ± 0.035	0.280 ± 0.056	0.335 ± 0.006

Table 1.2: *Measured πK S-wave scattering lengths for the isospin $I = 3/2$ state.*

reference	[BAKK70]	[CHO70]	[ANTI71]	[KIRS71]	[JONG73]	[ESTA78]
$a_{3/2}$	-0.085	-0.092	-0.078	-0.096	-0.072	-0.14 ± 0.07

Since the energy regions, where the amplitudes were measured, were not very close to threshold (approximately $m(\pi K) \sim 0.7 - 2$ GeV), the method as described in [LANG78] to obtain predictions for the low energy parameters, had to be used. Table 1.1 and 1.2 show the results for S-wave scattering lengths obtained by different analyses. Large fluctuations in these results and some inconsistency are evident.

Later experiments determined the behaviour of πK scattering near threshold using advanced methods based on dispersion relations. Unfortunately, the results are still not free from inconsistencies (see table 1.3).

Table 1.3: *πK scattering lengths determined by using dispersion relations.*

reference	[LANG77]	[JOHA78]	[KARA80]
$a_{1/2}$	0.237	0.240 ± 0.002	0.13 ± 0.09
$a_{3/2}$	-0.074	-0.05 ± 0.06	-0.13 ± 0.03

As can be seen from the results above, threshold parameters of πK scattering are barely known. According to table 1.3 containing data, evaluated by using dispersion relation techniques, the experimental values for $a_{1/2}$ lie in the range 0.13 to 0.24 and for $a_{3/2}$ in -0.13 to -0.05. This means, that these values are only known within a factor 2. New precise measurements of πK threshold parameters are badly needed in order to improve the understanding of πK processes. One possibility would be to measure the πK-atom lifetime and then to extract the difference $|a_{1/2} - a_{3/2}|$. In ref. [KARA80], exactly this scattering length combination was determined taking advantage of the forward sum rule and exploiting measured phase shifts. The allowed range of values was found to be $0.21 \leq a_{1/2} - a_{3/2} \leq 0.32$ $\left(M_{\pi^+}^{-1}\right)$. After 20 years and after tremendous progress in theory (ChPT), a direct as well as more precise measurement of this quantity is by far due. As pointed out in ref. [BERN91], more precise empirical information on the threshold parameters of πK scattering would give us a chance to test crucially the low-energy structure of QCD.

1.7 $A_{\pi K}$ atomic states as a source of model-independent data on πK S-wave scattering lengths

The by far dominant decay process for $A_{\pi K}$ atoms is:

$$A_{\pi K} \to \pi^0 + \overline{K^0}. \tag{1.12}$$

For $A_{\pi K}$ with principal quantum number n and orbital angular momentum l=0, the probability for this transition at leading order of isospin breaking is given by the following expression [BILE69]:

$$W_{n,0}(\pi^0\overline{K^0}) \approx \frac{8\pi}{9}\left(\frac{2\Delta m}{\mu}\right)^{1/2}(a_{1/2}-a_{3/2})^2|\Psi_{n,0}(0)|^2 + \cdots \approx \frac{1}{\tau_{n,0}} \tag{1.13}$$

where $\Delta m = (M_{K^-}+M_{\pi^+})-(M_{\pi^0}+M_{\overline{K^0}})$, $\mu = \dfrac{M_{K^-}\cdot M_{\pi^+}}{M_{K^-}+M_{\pi^+}}$ is the reduced atomic mass and $\Psi_{n,0}$ is the Coulomb wave function of $A_{\pi K}$ at zero distance. The ellipses denote isospin breaking corrections, which could be evaluated in the same way as done for the $A_{2\pi}$ decay probability [LUBO97, JALL99, IVAN99, GALL99, GASS99]. These corrections for $A_{\pi K}$ have not yet been worked out. Nevertheless, it is expected that they can be determined rather precisely improving the accuracy of eq. (1.13) to few % [GASS00]. Corrections to relation (1.13) in the $A_{2\pi}$ case have been studied also in a potential approach [MOOR95, GASH98], and the same procedure is applicable to $A_{\pi K}$.

Substituting the πK scattering length values from (1.8) into eq. (1.13), one obtains, at leading order in isospin breaking, the $A_{\pi K}$ lifetime in the ground state

$$\tau_{1,0} \equiv \tau = 4.7 \cdot 10^{-15} \text{ s}. \tag{1.14}$$

The Coulomb wave function is given by:

$$|\Psi_{n,0}(0)|^2 = \frac{p_B^3}{\pi n^3} \tag{1.15}$$

where p_B is the Bohr momentum of $A_{\pi K}$, $p_B = \alpha\mu$ and α is the fine structure constant. Using expression (1.13) and (1.15) one gets:

$$\tau_{n,0} = \tau_{1,0} \cdot n^3. \tag{1.16}$$

If the orbital angular momentum is $l > 0$, then annihilation is suppressed by a factor α^2 and the lifetimes of these states are larger by a factor $\sim 10^4$. Hence, $A_{\pi K}$ annihilation takes place practically only from $l = 0$ state with the lifetime given by eq. (1.16). By measuring the annihilation probability of the atom and knowing the distribution of $A_{\pi K}$ as a function of n, we obtain the lifetime τ and, finally, extract a value for $|a_{1/2} - a_{3/2}|$ [NEME85]. If the precision of τ is $\Delta\tau$, the relative uncertainty of $|a_{1/2} - a_{3/2}|$ will be:

$$\frac{\Delta(a_{1/2}-a_{3/2})}{|a_{1/2}-a_{3/2}|} \approx \frac{1}{2}\frac{\Delta\tau}{\tau}. \tag{1.17}$$

Therefore, if we measure τ with a precision of 20%, it will be possible to determine the value of the difference $|a_{1/2} - a_{3/2}|$ with a precision of 10%.

The energy difference between the atomic levels 2S and 2P consists of an electromagnetic component, $\Delta E^{em}_{2S-2P} = -0.29$ eV [KARI86] and a strong component $\Delta E^{S}_{2S-2P} \propto 2a_{1/2} + a_{3/2}$. By taking the πK scattering lengths from (1.8), we get $\Delta E^{S}_{2S-2P} = -0.9$ eV [EFIM87]. This latter difference is sensitive to the value of quark condensate and, in principle, can be experimentally measured [NEME85].

Chapter 2

$A_{\pi K}$ production in p-nucleus interaction at 24 GeV

The relations to calculate the production probabilities for $A_{2\pi}$, $A_{\pi K}$ and any other hydrogen-like atom, starting from the inclusive production cross-sections of the particles forming these atomic states, can be found in [NEME85]. In the same paper a method to observe these atoms and measure their lifetime is proposed. Estimates are given for the yields of atoms produced in pp-collisions at a beam energy of 70 GeV and an atom emission angle of 8.4° in the lab system. The experimental existence of $A_{2\pi}$ has been demonstrated at the U-70 accelerator [AFAN93] at Serpukhov in p-Ta collisions at $E_p = 70$ GeV and an emission angle of 8.4° in the lab system. This experiment allowed to estimate the $A_{2\pi}$ lifetime [AFAN94]. At present a precise determination (10%) of this lifetime is carried out by the DIRAC experiment at CERN.

The calculations by Nemenov [NEME85] have been extended to obtain the yields and momentum spectra of πK atoms in p-nucleus collision at E_p=24, 70 and 450 GeV for a set of angles from 1° to 6° [GORC00].

2.1 Basic relations

The cross-section of atom production is proportional to the double inclusive production cross-sections for the two constituents with small relative momentum. Atomic states can only be formed by two particles arising from short-lived sources (ρ, ω, $\Delta\ldots$), since their decay lengths are much smaller than the Bohr radius of the atom. In general, the differential production cross-section for such pairs is enhanced at small relative momenta, due to their Coulomb interaction in the final state. Therefore, they are called "Coulomb pairs".

There exists another category of pairs, which contain at least one particle from long-lived sources (η, η', Λ, K^0_s, $\Sigma^{\pm}\ldots$) with decay lengths much larger than the Bohr atomic radius. Hence they are not sensitive to the Coulomb and also not to strong interaction in the final state, and are called "non-Coulomb pairs".

The differential inclusive cross-section for $A_{\pi K}$ atom production can be written in the form [NEME85]

$$\frac{d\sigma^A_n}{d\vec{p}_A} = (2\pi)^3 \frac{E_A}{M_A} |\Psi_n(0)|^2 \left. \frac{d\sigma^0_s}{d\vec{p}_1 d\vec{p}_2} \right|_{\vec{p}_1 \approx \frac{M_\pi}{M_A}\vec{p}_A;\, \vec{p}_2 \approx \frac{M_K}{M_A}\vec{p}_A}, \tag{2.1}$$

where $\vec{p}_A$, E_A and M_A are the momentum, energy and mass of the atom in the lab system, respectively; $|\Psi_n(0)|^2 = p_B^3/\pi n^3$ is the square of the atomic wave function (without taking into account strong interaction between the particles forming the atom, i.e. pure Coulomb wave function), calculated at the origin for an atom of principal quantum number n and orbital angular momentum $l = 0$; p_B is the Bohr momentum of the particles forming the atom; $d\sigma_s^0/d\vec{p}_1 d\vec{p}_2$ is the double inclusive production cross-section for pairs from short-lived sources not considering the Coulomb final state interaction; $\vec{p}_1$ and $\vec{p}_2$ are pion and kaon momenta in the lab system, respectively. The momenta must obey with a very good approximation the relations: $\vec{p}_1 = \frac{M_\pi}{M_A}\vec{p}_A$ and $\vec{p}_2 = \frac{M_K}{M_A}\vec{p}_A$ (M_π and M_K are the masses of the two mesons). According to the n^{-3} behaviour of $|\Psi_n(0)|^2$, the atomic populations of the levels are: $W_{n=1} = 83.2\%$, $W_{n=2} = 10.4\%$, $W_{n=3} = 3.1\%$, $W_{n\geq 4} = 3.3\%$ and $\Sigma_{n=1}^{\infty}|\Psi_n(0)|^2 = 1.202|\Psi_1(0)|^2$ ([NEME85, AMIR99]).

Neglecting Coulomb interaction in the final state, the double inclusive cross-section has the form [GRIS82]:

$$\frac{d\sigma^0}{d\vec{p}_1 d\vec{p}_2} = \frac{1}{\sigma_{in}}\frac{d\sigma}{d\vec{p}_1}\frac{d\sigma}{d\vec{p}_2}R(\vec{p_1},\vec{p_2}), \tag{2.2}$$

where $d\sigma/d\vec{p}_1$ and $d\sigma/d\vec{p}_2$ are the pion and kaon inclusive cross-sections, σ_{in} is the inelastic cross-section of hadron production, R is a correlation function due to strong interactions in the final state..

The probability to produce a particle in the interaction (yield) can be obtained from the differential cross-section:

$$\frac{dN}{d\vec{p}} = \frac{d\sigma}{d\vec{p}}\frac{1}{\sigma_{in}}. \tag{2.3}$$

From eqs. (2.1), (2.2) and (2.3), after substituting the expression for $|\Psi_n(0)|^2$ and summing over n, one obtains an expression for the inclusive yield of atoms in all S–states from the inclusive yields of pions and kaons:

$$\frac{d^2N_A}{dp_A d\Omega} = 1.202 \cdot 8\pi^2(\mu\alpha)^3\frac{E_A}{M_A}\,\frac{p_A^2}{p_1^2\,p_2^2}\,\frac{d^2N_1}{dp_1 d\Omega}\,\frac{d^2N_2}{dp_2 d\Omega}R, \tag{2.4}$$

where $\mu = \frac{M_\pi M_K}{M_\pi + M_K}$ is the reduced mass of the $A_{\pi K}$, α is the fine structure constant, and Ω is the solid angle.

2.2 Comparison of experimental and calculated particle yields

We have used the program FRITIOF 6.0 [NILS87] to obtain the yields of π and K mesons. FRITIOF is a generator for hadron-hadron, hadron-nucleus and nucleus-nucleus collisions, and it makes use of JETSET 7.3 code [SJOS87] based on the Lund string fragmentation model.

A detailed test of the FRITIOF 6.0 results at the energy of 24 GeV has been made by comparing the calculated and the experimental yields of p, π^+, π^-, K^+ and K^-, reported in paper [EICH72], in the range of emission angles and momenta of our setup. The comparison shows that the deviation of the calculated yields from the data is less than 20%. Thus, the precision of the calculated yields of $A_{\pi K}$ and $A_{2\pi}$ is better than 40%.

Similar calculations performed with FRITIOF 7.02, the latest version of FRITIOF, show big disagreements for K^+, K^- and p yields. The p yield is the worst case, and since FRITIOF 6.0 fits well the experimental p data, we decided to use it for our calculations. This difference in the behaviour of the two programs can probably be explained by the fact, that FRITIOF 7.02 was developed for higher energies and higher $p_\perp$.

2.3 $A_{\pi K}$ and $A_{2\pi}$ yields

Using the particle yields calculated by FRITIOF 6.0 for the short-lived sources, we have obtained the distributions of the atom yields versus the atom momentum at different angles. The correlation coefficient, due to strong interaction for $\pi^+\pi^-$ pairs with same momenta, has the value $R = 1.65 \pm 0.05$ [GRIS82, URIB94]. For πK pairs, R is not known and is put to 1 in our calculations.

The yield for $A_{\pi K}$ in the present DIRAC setup is strongly suppressed by the geometry of the spectrometer, which is optimised to detect identical particles of equal momentum. Hence, it is necessary to tune the kaon spectrometer arm to higher momentum with respect to the pion arm. For this reason a rotation of the secondary (particle) channel and a rearrangement of the downstream detectors have to be performed. Moreover, this will make not possible to detect simultaneously $A_{\pi^+K^-}$ and $A_{\pi^-K^+}$. The detection of $A_{\pi^+K^-}$ is more clean, since the detection of the corresponding antiatom ($A_{\pi^-K^+}$) shows a much less favourable signal-to-background ratio [ADEV95]. Therefore, all following calculations and studies, concerning a modified experimental setup, have been focused on the detection of $A_{\pi^+K^-}$.

The results of the simulations are presented in fig. 2.1–2.3. In fig. 2.1 the yields of $A_{\pi^+K^-}$ are shown for the reaction $p+\mathrm{Ni} \to A_{\pi^+K^-}+X$ at the proton energy $E_p = 24$ GeV for the present setup and for the modified one. The corresponding values for $A_{K^+\pi^-}$ and $A_{2\pi}$ are shown in fig. 2.2 and 2.3, respectively.

In table 2.1 the yields of $A_{2\pi}$, $A_{\pi^+K^-}$ and $A_{K^+\pi^-}$ are shown for the present setup and two setup modifications: rearrangement of only downstream detectors and rotation of both secondary channel and downstream detectors (referred as "modified" setup). It is worth to note that both $A_{\pi^+K^-}$ *and* $A_{K^+\pi^-}$ can be detected by the present setup. On the other hand an asymmetrical setup geometry can only be optimised for the detection of *either* $A_{\pi^+K^-}$ *or* $A_{K^+\pi^-}$. The yield of $A_{\pi^+K^-}$ as a function of the magnetic field is presented in table 2.2.

Table 2.1: *Yields of detected* $A_{2\pi}$, $A_{\pi^+K^-}$ *and* $A_{K^+\pi^-}$ (N_A *per 1* $p-Ni$ *interaction*) *calculated for different modifications of the setup.*

Setup modification	Present setup	Rotated detectors	Both channel and detectors rotated
$A_{2\pi}$	$1.8 \cdot 10^{-9}$	$1.4 \cdot 10^{-9}$	$2.5 \cdot 10^{-10}$
$A_{\pi^+K^-}$	$1.8 \cdot 10^{-11}$	$5.2 \cdot 10^{-11}$	$5.8 \cdot 10^{-11}$
$A_{K^+\pi^-}$	$3.2 \cdot 10^{-11}$	$9.6 \cdot 10^{-11}$	$10.5 \cdot 10^{-11}$

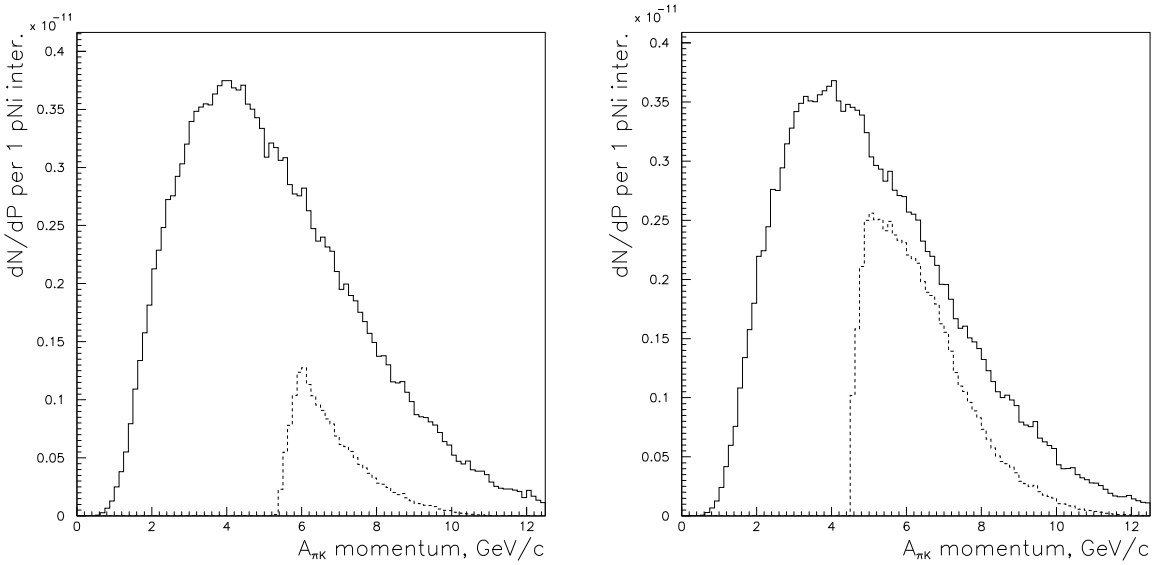

Figure 2.1: *Yields of $A_{\pi^+K^-}$ for the reaction $p + \mathrm{Ni} \to A_{\pi^+K^-} + X$ at the proton energy $E_p = 24$ GeV as a function of the atom momentum. Solid lines show $A_{\pi^+K^-}$ emitted into the angular aperture of the secondary channel. Dashed lines refer to atoms detected by the DIRAC setup (all atoms ionised). The left figure corresponds to the present setup, the right one to the modified setup.*

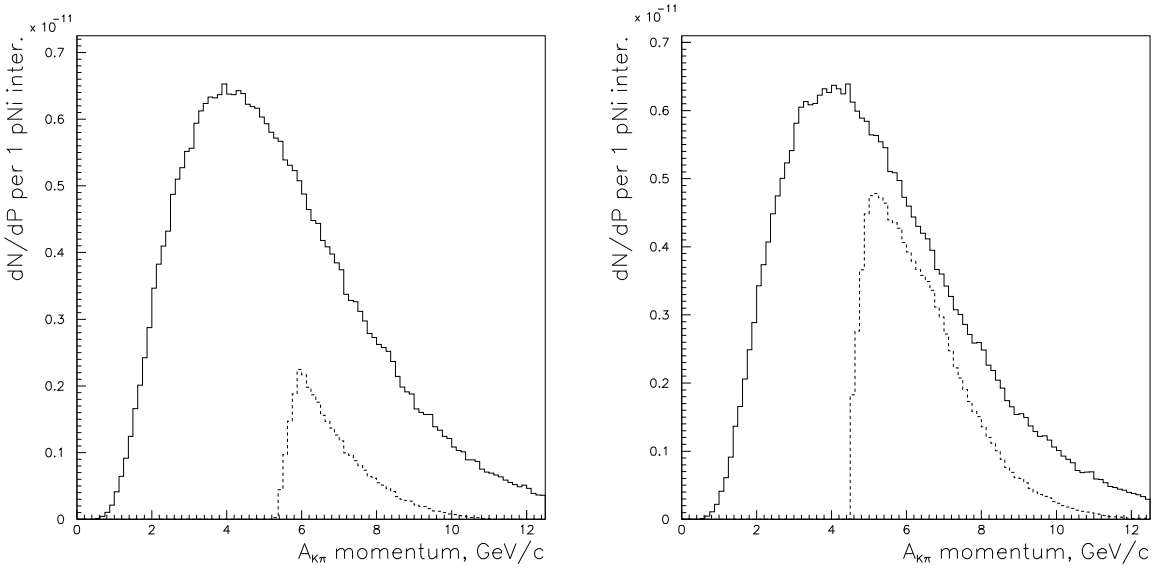

Figure 2.2: *Yields of $A_{K^+\pi^-}$ for the reaction $p + \mathrm{Ni} \to A_{K^+\pi^-} + X$ at the proton energy $E_p = 24$ GeV as a function of the atom momentum. Solid lines show $A_{K^+\pi^-}$ emitted into the angular aperture of the secondary channel. Dashed lines refer to atoms detected by the DIRAC setup (all atoms ionised). The left figure corresponds to the present setup, the right one to the modified setup.*

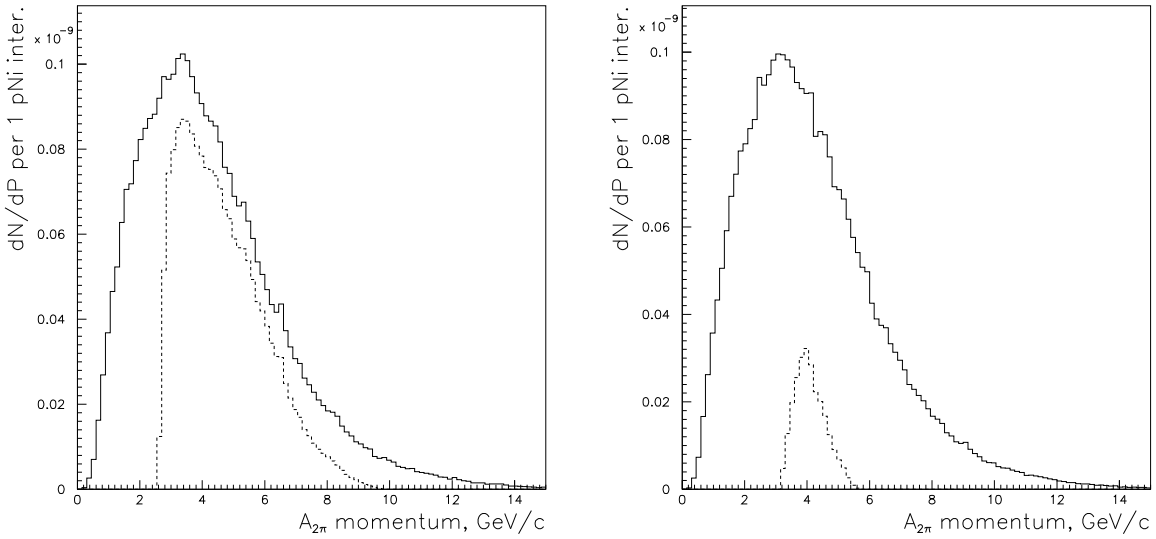

Figure 2.3: *Yields of $A_{2\pi}$ for the reaction $p + \mathrm{Ni} \to A_{2\pi} + X$ at the proton energy $E_p =$ 24 GeV as a function of the atom momentum. Solid lines show $A_{2\pi}$ emitted into the angular aperture of the secondary channel. Dashed lines refer to atoms detected by the DIRAC setup (all atoms ionised). The left figure corresponds to the present setup, the right one to the modified setup.*

Table 2.2: *Yield of $A_{\pi^+K^-}$ (N_A per 1 $p-Ni$ interaction), detected by the modified setup as a function of the magnetic field ($H_0 = 1.65$ T is the current value of the magnetic field).*

H/H_0	1.0	0.9	0.8	0.7	0.6
$A_{\pi K}$	$5.8 \cdot 10^{-11}$	$6.2 \cdot 10^{-11}$	$6.4 \cdot 10^{-11}$	$6.3 \cdot 10^{-11}$	$5.7 \cdot 10^{-11}$

Chapter 3

Detection of relativistic $A_{\pi K}$ and lifetime measurement

The method for detecting $A_{\pi K}$ is based on the observation of πK pairs from the atom breakup (ionisation) which occurs in the production target. The main feature of these "atomic pairs" is their low relative momentum in the centre of mass system ($Q <$ 4 MeV/c). For a given target thickness and $A_{\pi K}$ momentum, the breakup probability of the πK atom is a unique function of τ, the lifetime in the ground state (see chapter 4). Therefore, the measurement of this breakup probability allows to investigate the atom lifetime [NEME85].

The breakup probability is the ratio between the number of ionised and the number of produced $A_{\pi K}$: $P_{\rm br} = n_A/N_A$. The value of n_A can be extracted from the analysis of the experimental Q-distribution of all free and atomic πK pairs, whereas the value of N_A is related to the number of free pairs with low relative momentum.

The Q distribution of all πK pairs, produced in proton-nucleus interactions in the target, is described in the form:

$$\begin{aligned} dN/dQ &= dN_{\rm real}/dQ + dn_A/dQ, \\ dN_{\rm real}/dQ &= dN^{\rm long}_{\rm real}/dQ + dN^{\rm short}_{\rm real}/dQ \end{aligned} \tag{3.1}$$

where Q is the relative momentum in the πK centre of mass system, and $N^{\rm short}_{\rm real}$ is the number of πK pairs originating from short-lived sources (ρ, K^*, ϕ, fragmentation,...: fig. 3.1c). These pairs are called "Coulomb pairs" because of the significant Coulomb and also strong interaction in the final state. The quantity $N^{\rm long}_{\rm real}$ is the number of πK pairs with at least one particle originating from long-lived sources (η, η',...), where no significant final state interaction takes place — thus they are called "non-Coulomb pairs" (fig. 3.1b). Finally, n_A is the number of πK pairs as a result of the ionisation or breakup of $A_{\pi K}$.

Accidental πK pairs are uncorrelated in time (fig. 3.1a), i.e. they are neither affected by Coulomb nor strong interaction in the final state. Hence, they can be used to describe the distribution of free πK pairs. If we denote $dN_{\rm acc}/dQ \equiv \Phi(Q)$, the Q distribution of accidental pairs, then the distribution of real πK pairs, $dN_{\rm real}/dQ$, can be approximated as follows:

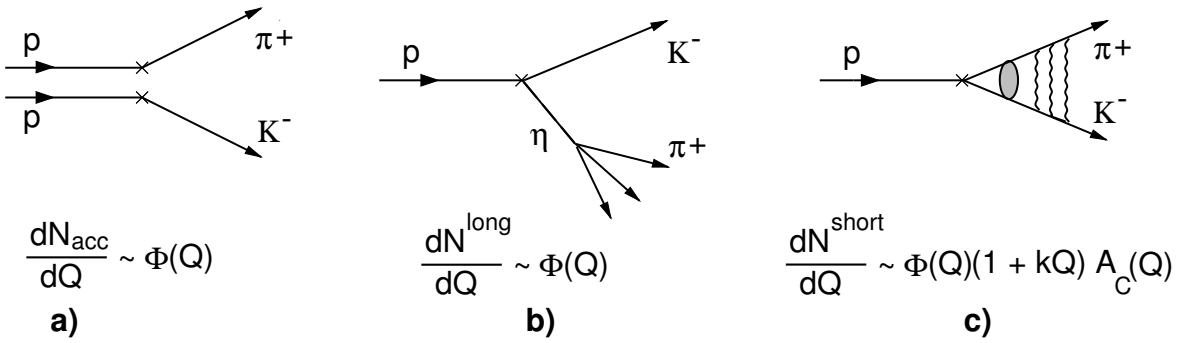

Figure 3.1: *Production diagrams of accidental pairs a), of pairs from long-lived sources b) and of pairs from short-lived sources c). Accidental pairs and pairs originating from long-lived sources have the same relative Q distribution.*

$$\begin{aligned} dN_{\rm real}/dQ &= \underbrace{A\Phi(Q)}_{\rm long} + \underbrace{B\Phi(Q)(1+kQ)A_C(Q)}_{\rm short} = \\ &= B\Phi(Q)\left[(1+kQ)A_C(Q)+f\right], \qquad f = A/B \end{aligned} \tag{3.2}$$

where the terms $(1+kQ)$ and $A_C(Q)$ take into account strong and Coulomb final-state interaction, respectively [SAKH48]. The Coulomb correlation function, $A_C(Q)$, is known from theory with a precision of $\sim 0.5\%$ [BAYE69], whereas B, k, f are free parameters, and $\Phi(Q)$ is the measured spectrum of accidentals.

The experimental distribution $dN_{\rm real}/dQ$ of real πK pairs will be fitted by the function (3.2) for values $Q > 4$ MeV/c, where no atomic pairs are expected. The values of the fit parameters B, k and f are then used to determine the total number of free pairs ($N_{\rm real}$) in the region $0 \le Q \le 3$ MeV/c. Finally, the number of atomic pairs n_A in the interval $0 \le Q \le 3$ MeV/c is obtained by subtracting $N_{\rm real}$ from the total number of πK pairs collected in this interval. The Q distribution of atomic pairs can be theoretically predicted and used to determine the total number of atomic pairs for any value of Q:

$$n_A = n_A(Q \le 3 \text{ MeV/c}) + n_A(Q > 3 \text{ MeV/c}). \tag{3.3}$$

From the best value of the fit parameters B and k, we can also determine the total number of Coulomb pairs ($N_{\rm real}^{\rm short}$) in the region $0 \le Q \le 3$ MeV/c. The strong part in the production of Coulomb pairs with $Q \le 3$ MeV/c as well as in the production of $A_{\pi K}$ is the same (fig. 3.2) and so cancels out in the ratio $N_A/N_{\rm real}^{\rm short}$. Therefore, the number of produced $A_{\pi K}$, N_A, can be determined from the model-independent ratio between bound

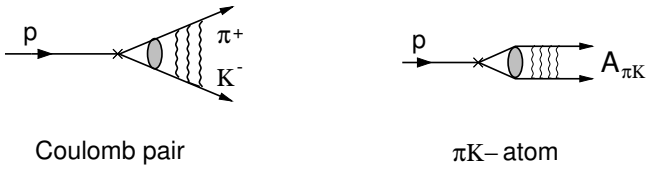

Figure 3.2: *Diagrams of Coulomb pairs and $A_{\pi K}$. Both have the same strong production contribution for $Q \le 3$ MeV/c*

πK pairs and continuum pairs [AFAN97, AFAN99A], *i.e.* via the relation:

$$N_A = 0.665 \cdot N_{\rm real}^{\rm short}(Q \leq 3 \text{ MeV/c}) \tag{3.4}$$

This procedure was used in our previous experiment, where first experimental evidence for $A_{2\pi}$ was found and a lifetime estimation was made [AFAN93].

The lifetime dependence of the $A_{\pi K}$ breakup probability $P_{\rm br}^{\rm theor}$ can be calculated with a precision $\sim 1\%$ for any target (see next chapter). The $A_{\pi K}$ lifetime, τ, will be determined by comparing the measured value, $P_{\rm br}^{\rm exp} = n_A/N_A$, with the theoretical curve ($P_{\rm br}^{\rm theor}$).

Chapter 4

Interaction of relativistic πK atoms with matter

The interaction of the hydrogen-like relativistic atoms, formed by elementary particles, with the material of the production target is the key point for the observation and lifetime measurement of these atoms. In the approach proposed by Nemenov [NEME85], the atoms are detected via the low relative momentum pairs, produced from atom breakup (ionisation). To obtain the atom lifetime one has to measure the ratio between the number of "ionised atoms" and the number of produced atoms (called the atom breakup probability) and then to use the calculated dependency of $P_{\rm br}$ on the lifetime. In order to get a precise evaluation of the atom lifetime it is crucial to perform an accurate calculation of the atom breakup probability in target materials.

The method to relate the breakup probability with the atom lifetime was originally developed for $\pi^+\pi^-$ atoms [AFAN93, AFAN94, ADEV95] and consists of two main steps:

— calculation of the interaction cross-sections of the relativistic hydrogen-like atoms with ordinary atoms;

— description of the evolution of the atom state population, as it traverses the target to evaluate the breakup probability.

In this chapter we shortly describe the application of this method to πK atom. The results on the breakup probability allow to select the optimal target for the $A_{\pi K}$ observation and lifetime measurement.

4.1 $A_{\pi K}$ interactions with target atoms

After production in hadron-nucleus interaction, $A_{\pi K}$ interacts with the atoms of the target material, in which they are travelling. The electromagnetic cross-sections of the $A_{\pi K}$ ground state with target atoms are of the order of 10^{-21} cm^2 (1 kbarn). Strong interaction cross-sections are much smaller and can be neglected.

Since the electromagnetic interaction depends on the charge as Z^2, the cross-section with the atom electrons is Z times smaller than with nuclei. Indeed exact calculations, performed for interactions of πK atoms with different materials [AFAN91], show that the precision of this simple estimation is sufficient. For target materials with Z about 30, which are considered below, the correction due to $A_{\pi K}$ electromagnetic interaction

with electrons (the so-called incoherent scattering) leads to a cross-section increase of $\sim$2%. In the following we do not take into account this contribution, but for more precise calculations it should be considered (see also the following remark about Hartree–Fock calculations).

The projectile atom interacts dominantly with the electric field of the target atoms (Coulomb interaction). The interaction via the magnetic field arising due to the Lorentz boost is small enough. In ref. [MROW87, DENI87], it has been shown that for the interaction of relativistic $A_{\pi K}$ with Cu the total cross-section of the magnetic interaction compared with the electric one is 0.8% only, and hence is not considered here.

To describe the Coulomb interaction of the $A_{\pi K}$ with the target atoms, we use the first Born approximation [AFAN96], considering only single photon exchange. For these calculations the form factors of arbitrary discrete-discrete transitions of a hydrogen-like atom have been derived in a closed analytical form [AFAN93A, AFAN96]. The precision of this approach is of the order $(Z\alpha)^2$. Hence, this leads to an accuracy of 4% for target materials with Z about 30. For $A_{2\pi}$ the total cross-sections have been calculated more accurately using the Coulomb-modified Glauber approximation [TARA91, AFAN99, IVAN99A]. This allows to take into account all multi-photon exchanges and provides a much higher accuracy. It has been shown [AFAN99], that following this approach, all the computed cross-sections are smaller than those evaluated in the Born approximation. The difference ranges from 1.5% for titanium ($Z = 22$) up to 14% for tantalum ($Z = 73$). Thus, the accuracy of the first Born approximation is sufficient for low-Z target materials, discussed below. Nevertheless, additional calculations, using the Glauber approach, are in progress.

The calculation accuracy of the electromagnetic cross-sections depends also on the precision the form factors of target atoms. In our calculation [AFAN96] we use the Moliere parametrisation of the Thomas–Fermi potential (TFM) [MOLI47]. However, more accurate representations of these form factors, based on the self-consistent field method of Hartree–Fock [HUBB75, HUBB79, SALV87], are available. Calculations of $A_{\pi K}$ interaction with various materials, performed using both methods [AFAN91], have shown that the cross-sections, calculated with the TFM parametrisation, are larger by $\sim 1\%$ for the $A_{\pi K}$ ground state and slightly more for the excited states than those obtained using the Hartree–Fock approach. On the other hand, since we neglect the incoherent part of the interactions, which is of the same order of magnitude, the total uncertainty of the calculated cross-section does not exceed $1 \div 2\%$, at least for the low lying states of $A_{\pi K}$.

In a recent paper [HALA99], cross-sections for $\pi^+\pi^-$ atoms have been calculated using Hartree–Fock form factors at first-order of perturbation theory. For a Ni target, the difference between these cross-sections and our calculations [AFAN96] varies from -1%, for the ground state, up to 15% for states with principal quantum number $n = 10$. In spite of such large difference (see [HALA99] for discussion), the $A_{2\pi}$ breakup probability, calculated with both sets of cross-sections [AFAN00], differs only by 0.6%. Therefore, one can conclude that only the cross-section accuracy for low lying atomic states is significant for a precise determination of the atom breakup probability.

4.2 Passage of $A_{\pi K}$ through the target material and target choice

In this section we shortly describe the procedure to calculate the $A_{\pi K}$ breakup probability, using the method developed for $A_{2\pi}$ [AFAN96]. There will be given some numerical results in order to select the target material.

Using the calculated total and excitation cross-sections, the evolution of the atomic state populations during πK atom passage through the target can be described by a set of differential equations. The lifetime and momentum of $A_{\pi K}$ are parameters of this set of equations. Since the atom can get excited or deexcited in the interaction, an exact solution for any state may only be obtained as a solution of the infinite set of equations. However, since the most probable transitions are between nearest states, we can establish an upper limit to the number of equations without affecting significantly the accuracy of the result. Thus we have considered only states with principal quantum number $n \leq 10$. In this limit the number of states, having a non-zero population (in the first Born approximation), is 220. The populations of all states, with principal quantum number $n \leq 10$, as a function of the target thickness have been found by solving the set of differential equations. These quantities takes into account $A_{\pi K}$ interaction with the target atoms and $A_{\pi K}$ annihilations.

The sum of these populations gives the probability for $A_{\pi K}$ to survive in one of the finite states with $n \leq 10$, P_{fin}. The total populations of all other atomic states with $n > 10$, P_{tail}, has been estimated extrapolating from the populations calculated for $n \leq 10$. Since πK atoms annihilate dominantly from 1S state [NEME85] and the population of the first few states is known with high accuracy, the probability of $A_{\pi K}$ annihilation P_{anh} is known very precisely. Having calculated the probabilities for $A_{\pi K}$ to survive or to annihilate, the remainder is the $A_{\pi K}$ breakup probability P_{br}:

$$P_{\text{br}} = 1 - P_{\text{fin}} - P_{\text{tail}} - P_{\text{anh}}. \tag{4.1}$$

The accuracy of the P_{br} calculation is estimated to be not worst than 0.5%. In this way, the $A_{\pi K}$ breakup probability can be calculated in any target as a function of the atom momentum and lifetime. All the results presented below are obtained with this procedure. For a detailed discussion about the procedure accuracy, see [ADEV95, AFAN96].

In all calculations the $A_{\pi K}$ momentum has been fixed to the value 6.5 GeV/c, which corresponds to the mean momentum of the atoms, entering the experimental setup. The calculations have been performed for the set of targets, already used by the DIRAC experiment. Their thickness was selected in order to provide the same multiple scattering contribution.

In fig. 4.1 the $A_{\pi K}$ breakup probability is shown as a function of the atom lifetime for several targets. Fig. 4.2 shows the lifetime dependence of the relative uncertainty, $\Delta P_{\text{br}}/P_{\text{br}}$, corresponding to a 20% accuracy in the determination of the $A_{\pi K}$ lifetime. The number of produced $A_{\pi K}$, which can provide the required accuracy, can be roughly estimated to be proportional to $(\Delta P_{\text{br}}/P_{\text{br}})^{-2}$. Fig. 4.3 shows the lifetime dependence on the number of produced πK atoms, necessary to get the same accuracy in the lifetime measurement for all targets. It can be used to select the most adequate target for the lifetime measurement.

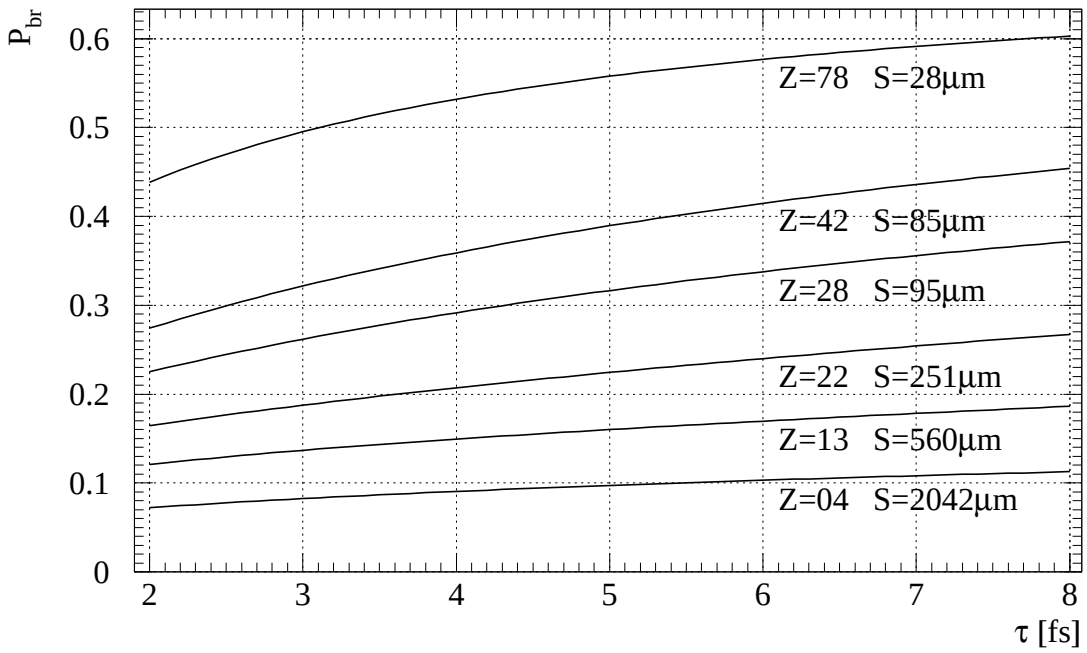

Figure 4.1: *$A_{\pi K}$ breakup probability as a function of the atom lifetime for different targets with the nucleus charge Z and the target thickness S.*

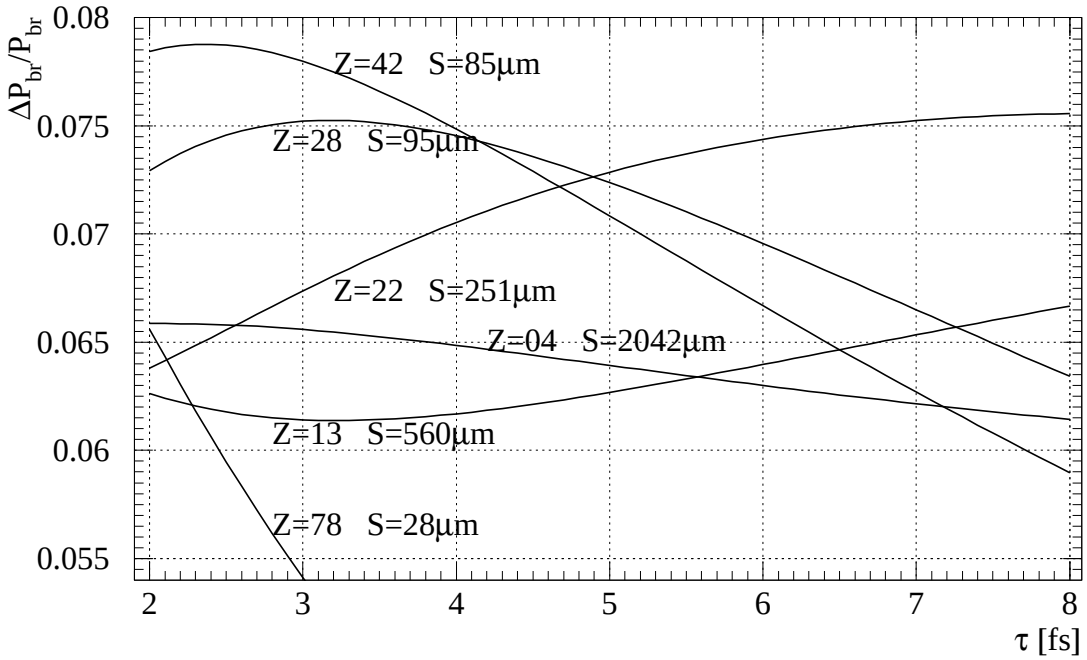

Figure 4.2: *Relative accuracy, necessary for the breakup probability, $\Delta P_{\rm br}/P_{\rm br}$, to obtain the $A_{\pi K}$ lifetime with a precision of 20%, versus the atom lifetime, for different targets.*

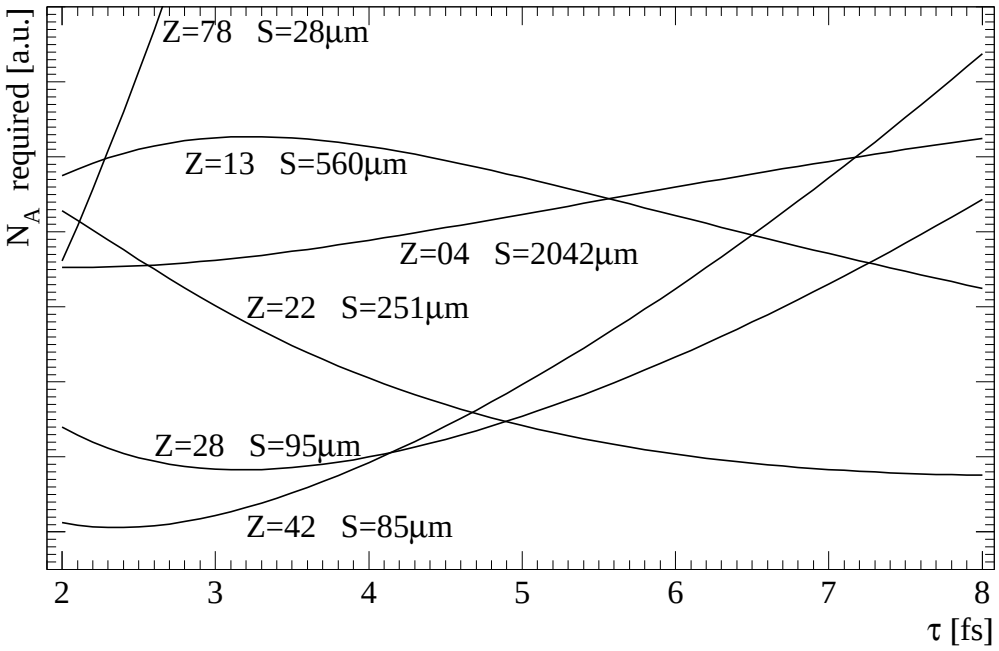

Figure 4.3: *Number of $A_{\pi K}$, versus the atom lifetime, necessary to provide the same accuracy in the lifetime measurements, for different targets.*

The $P_{\rm br}$ dependence on the atom momentum shown in fig. 4.4 illustrates that all above results will not change significantly if the average $A_{\pi K}$ momentum will differ from the value used in the above calculation.

Table 4.1 shows some numerical results. For different target materials with nucleus charge Z and for the $A_{\pi K}$ ground state the total cross-sections $\sigma_{\rm 1S}^{tot}$ and the corresponding interaction lengths $\lambda_{\rm int}$ are given. The calculations have been done assuming the $A_{\pi K}$ lifetime $4.7{\cdot}10^{-15}$ s and the $A_{\pi K}$ momentum of 6.5 GeV/c, corresponding to an annihilation length $\lambda_{\rm anh} = 15.1\,\mu$m. For a given target thickness S, the following numbers are reported: the total population $P_{\rm fin}$ of all states with $n \leq 10$, the "tail" population $P_{\rm tail}$, the $A_{\pi K}$ annihilation $P_{\rm anh}$ and breakup $P_{\rm br}$ probabilities, and the relative uncertainty $\Delta P_{\rm br}/P_{\rm br}$ to obtain the lifetime with 20% accuracy.

From fig. 4.1 one can conclude, that the Pt target seems to be most suitable for the $A_{\pi K}$ observation, since it provides the highest yield of "atomic pairs". Figures 4.2 and 4.3 show, that for the expected value of the $A_{\pi K}$ lifetime around $5 \cdot 10^{-15}$ s, the Ti, Ni and

Table 4.1:

	Z	$\sigma_{\rm 1S}^{tot}$ cm^2	$\lambda_{\rm int}$ μm	S μm	$P_{\rm fin}$	$P_{\rm tail}$	$P_{\rm anh}$	$P_{\rm br}$	$\Delta P_{\rm br}/P_{\rm br}$
Be	04	$6.14{\cdot}10^{-23}$	1307	2042	0.020	$3.8{\cdot}10^{-4}$	0.885	0.095	$6.4{\cdot}10^{-2}$
Al	13	$5.94{\cdot}10^{-22}$	278	560	0.041	$4.9{\cdot}10^{-4}$	0.801	0.157	$6.2{\cdot}10^{-2}$
Ti	22	$1.63{\cdot}10^{-21}$	107	251	0.067	$5.8{\cdot}10^{-4}$	0.713	0.219	$7.2{\cdot}10^{-2}$
Ni	28	$2.59{\cdot}10^{-21}$	41.9	95	0.131	$8.3{\cdot}10^{-4}$	0.559	0.310	$7.3{\cdot}10^{-2}$
Mo	42	$5.63{\cdot}10^{-21}$	27.4	85	0.125	$7.3{\cdot}10^{-4}$	0.493	0.381	$7.2{\cdot}10^{-2}$
Pt	78	$1.84{\cdot}10^{-20}$	8.14	28	0.199	$1.0{\cdot}10^{-3}$	0.249	0.551	$4.1{\cdot}10^{-3}$

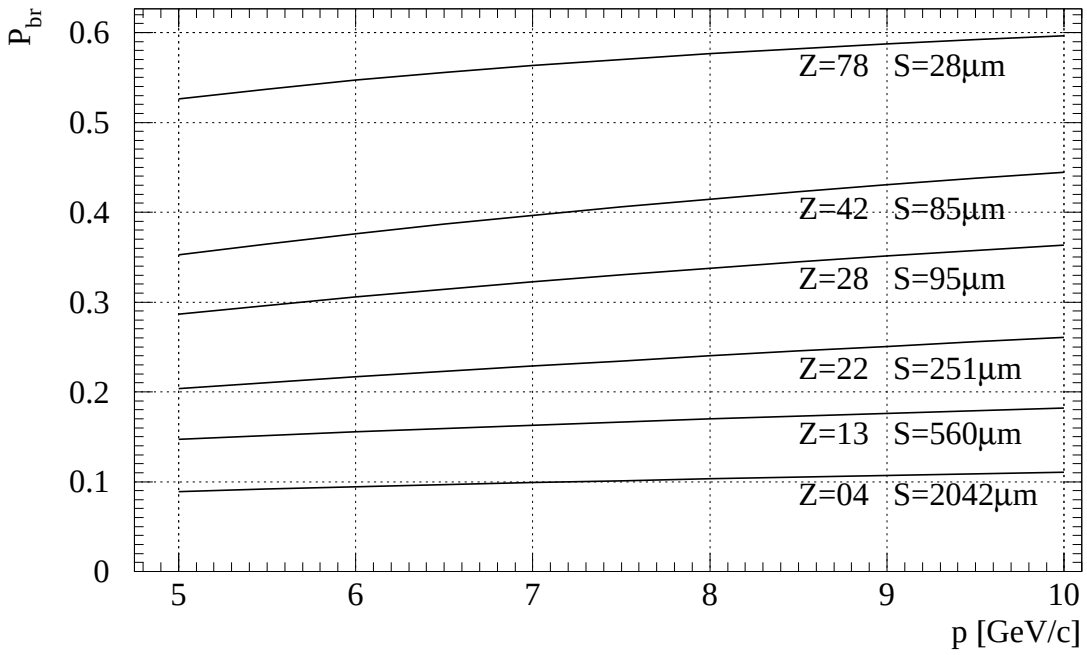

Figure 4.4: *$A_{\pi K}$ breakup probability as a function of the atom momentum for the $A_{\pi K}$ lifetime fixed to $4.7 \cdot 10^{-15}$ s.*

Mo targets provide almost equal sensitivities for the lifetime measurement. Moreover, with these three targets, a comparable statistics is required to measure the $A_{\pi K}$ lifetime with the desired accuracy in a range of the lifetimes much wider than the theoretically estimated uncertainty.

The sensitivities for the lifetime measurement are almost the same for $A_{2\pi}$ and $A_{\pi K}$: the value $\Delta P_{\rm br}/P_{\rm br} = 7 \cdot 10^{-2}$, obtained for $A_{2\pi}$ produced in Ni target, can be compared to the corresponding value, shown in the last column of table 4.1 for $A_{\pi K}$.

4.3 Relative momentum distribution of "atomic pairs"

The precise knowledge of the relative momentum distribution for the pairs, originating from the atom breakup ("atomic pairs") is crucial in order to determine the overall number of produced πK atoms in the target. Fig. 4.5 shows distributions for 1S and 2S states for $A_{2\pi}$ and $A_{\pi K}$, calculated in a dipole approximation. These distributions reflect the momentum distributions before the atom breakup. Those from excited states are narrower than those from the ground one, and the $A_{\pi K}$ spectra are wider than the corresponding $A_{2\pi}$ ones, because of the higher Bohr momentum for $A_{\pi K}$.

However, the initial distributions are significantly modified by multiple scattering inside the target. Results of a simulation for $A_{2\pi}$ show, that only the 1S distribution contributes to the width of the total distribution, whereas the effect of the other states is completely invisible. For $A_{\pi K}$ the final momentum distribution will be even wider. Hence, the atomic πK pairs will be spread over a larger range of relative momenta, and the effect of "background", associated to free pairs, will be larger. This point sets a limit on the possibility to use thicker targets, to get more "atomic pairs".

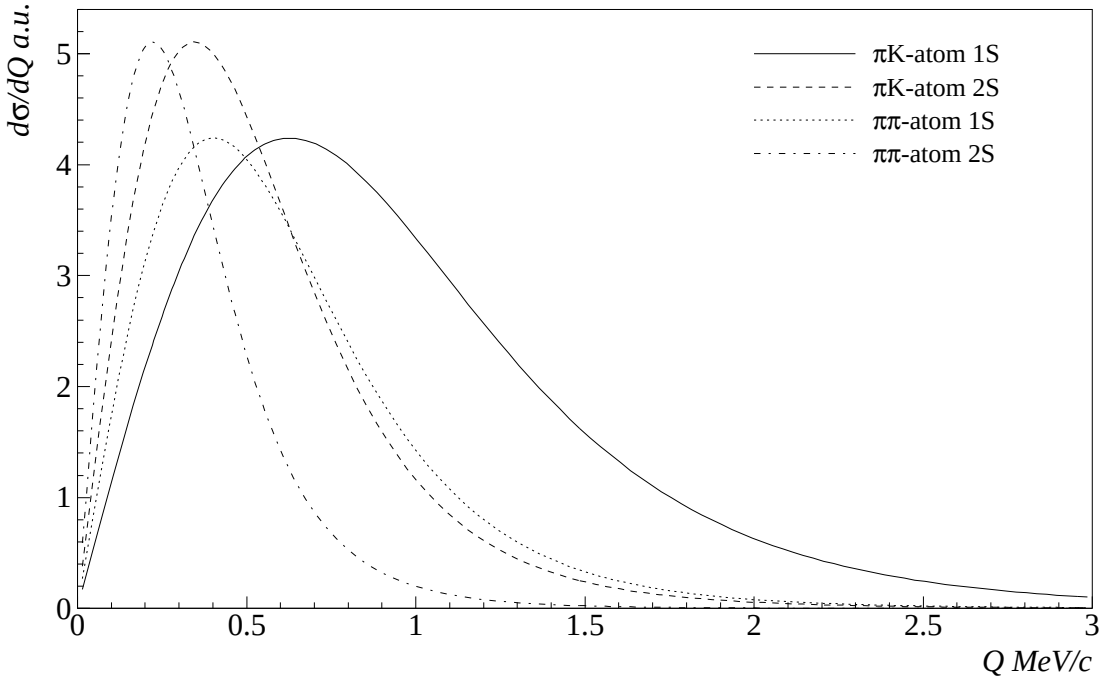

Figure 4.5: *Relative momentum distributions for pairs from atom breakup for $\pi^+\pi^-$ and πK-atoms, being initially in 1S and 2S states.*

Chapter 5

The present DIRAC setup

5.1 General description

The aim of the DIRAC experiment is to detect $\pi^+\pi^-$ pairs with very small opening angles and therefore is designed to measure their relative momentum with high precision $\sim$ 1 MeV/c. To accomplish this task a double arm magnetic spectrometer was commissioned during October – November 1998 at the T8 experimental area of the CERN PS East Hall (fig. 5.1).

The proton beam intensity can be varied from $0.5 \cdot 10^{11}$ to $3 \cdot 10^{11}$ protons per spill; the proton spill length is $\approx$ 0.4 s; the beam dimensions in the vertical and horizontal planes are 2 and 3 mm at 2σ, respectively, and the beam has no large halo. The East Hall radiation shielding allows to withstand average beam intensities up to $2.7 \cdot 10^{10}$ protons per second.

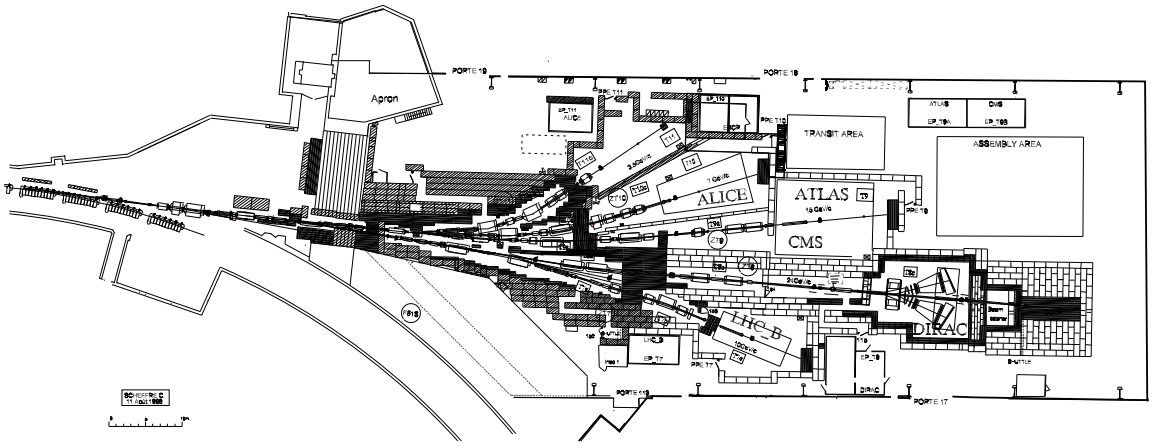

Figure 5.1: *East Hall general view.*

A view of the DIRAC setup inside the radiation shielding is shown in fig. 5.2. A top view of the setup with indication of the different components is shown in fig. 5.3.

The magnetic spectrometer is arranged on a secondary particle channel, inclined upwards by 5.7° with respect to the incoming proton beam direction (fig. 5.5), and the channel aperture is 1.2 msr. The 24 GeV/c PS proton beam entering the DIRAC

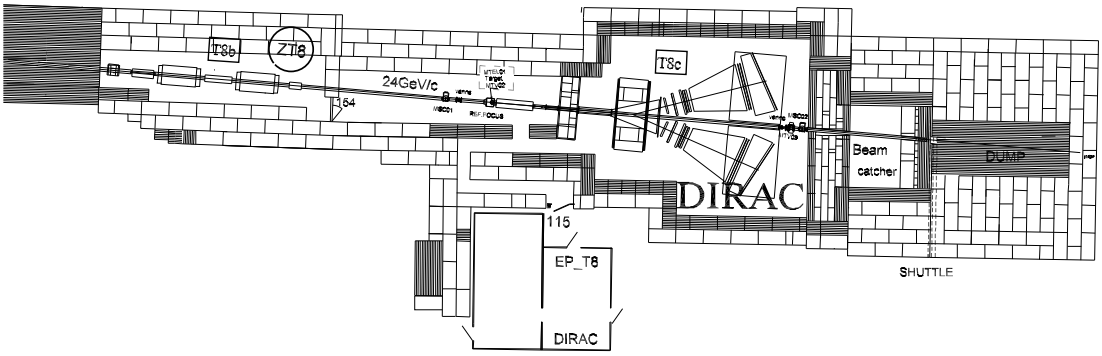

Figure 5.2: *The DIRAC setup and the radiation shielding.*

experimental setup encounters the nuclear target station, where $A_{2\pi}$ atoms are produced. This system consists of several target materials (Be, Al, Ti, Ni, Mo, Pt and Pb), that can be placed alternatively across the beam by rotating a remotely controlled support device.

To track the produced pion pairs, a first set of detectors is placed upstream of the spectrometer magnet:

— 4 planes of MicroStrip Gas Chambers (MSGC) with Gas Electron Multiplier (GEM);

— a Scintillating Fibre Detector (SFD);

— an Ionisation Hodoscope (IH).

The $\pi^+\pi^-$ pairs are then bent in the horizontal plane by a dipole magnet (1.65 T). Downstream the magnet two identical detector arms have been constructed both including the following detectors:

— 4 modules of Drift Chambers (DC1–DC4);

— a Vertical Hodoscope (VH);

— a Horizontal Hodoscope (HH);

— a threshold gas Cherenkov counter (C);

— a Preshower counter (PSh);

— a Muon identification system (Mu).

The top, side and isometric views of the DIRAC setup are shown in figs. 5.4, 5.5 and 5.6.

5.2 The DIRAC sub-detectors

5.2.1 Detectors upstream of the magnet

The Microstrip Gas Chambers

The detector consists of 4 planes of MSGC with GEM. The four planes have an orientation of 0°, 90°, 5° and 85° in the plane perpendicular to the secondary beam axis. The total number of channels is 2048. Each chamber has a gas gap of 6 mm divided into two 3 mm regions by means of a GEM foil with a 140 μm pitch pattern of holes with 50/70 μm (internal/external) hole diameters. The microstrip plate is made of 200 μm pitch Chromium strips on a bare Desag D263 glass, with 9 μm and 100 μm anode and cathode width, respectively. The gas employed is a mixture of Ar–DME.

The front end electronics currently used is the APC64 [HORI93, GOME97] with analog readout.

The number of detector dead channels is around 1% and no significant deterioration due to radiation has been observed since their installation. The efficiency for a standard detector is around 93% , and single hit resolution is 54 μm. This detector is important to get a resolution in the transverse components of the pion pair c.m.s. relative momentum below 1 MeV/c, thus providing high resolution tracking upstream the magnet.

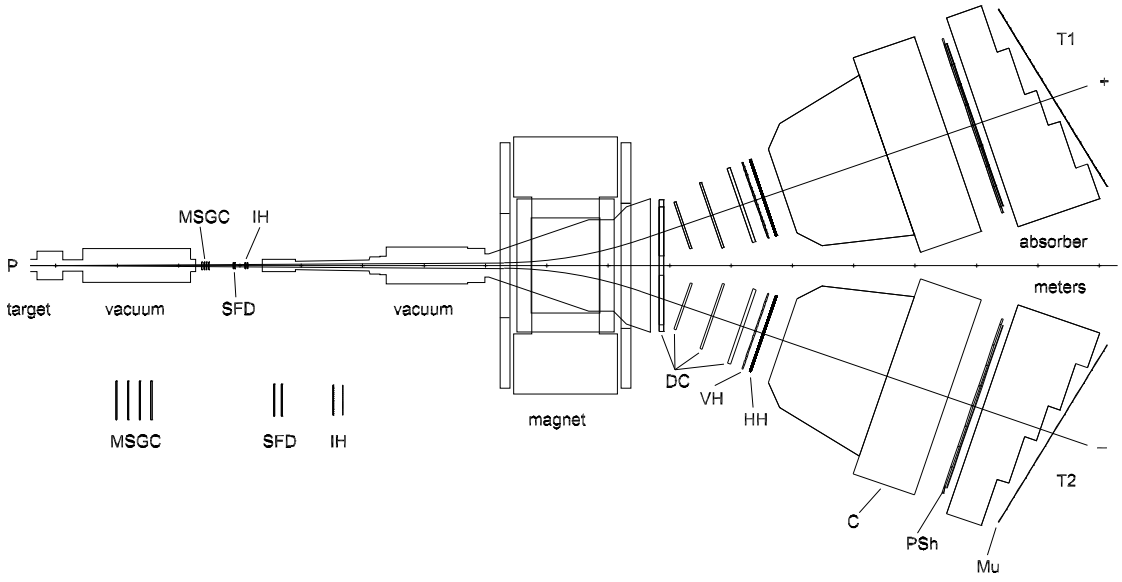

Figure 5.3: *Schematic top view of the DIRAC spectrometer. Moving from the target station toward the magnet there are: four MicroStrip Gas Chamber (MSGC), two Scintillating Fibre Detectors (SFD) and an Ionisation Hodoscope (IH). Downstream the dipole magnet, on each arm of the spectrometer, are located: 4 modules of Drift Chambers (DC), a Vertical and a Horizontal Hodoscope (VH, HH), a Cherenkov counter (C), a Preshower detector (PSh) and, behind an iron absorber, a Muon counter (Mu).*

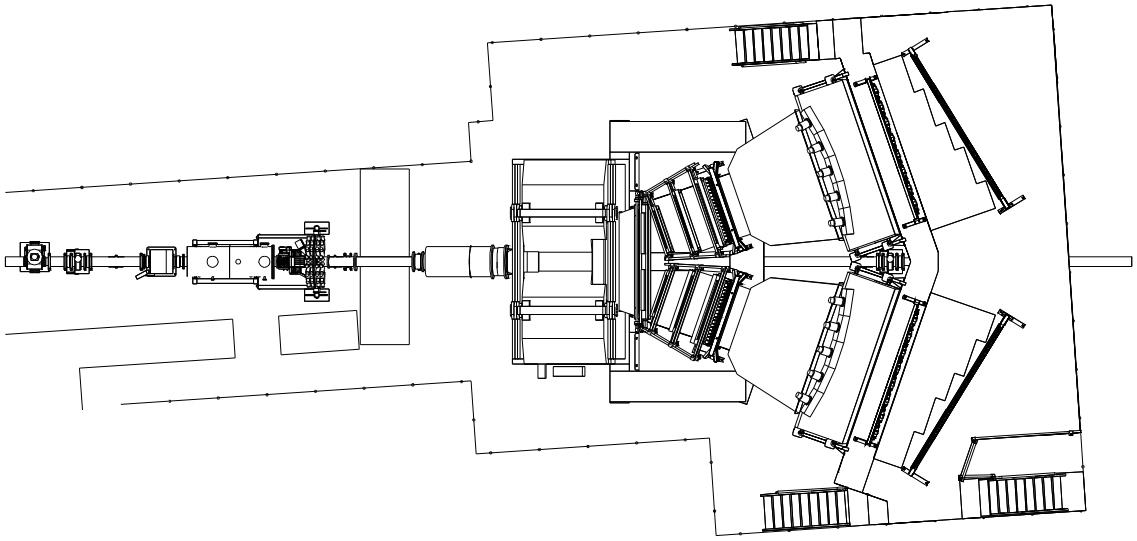

Figure 5.4: *Setup top view with the radiation shielding boundaries (each division corresponds to one meter).*

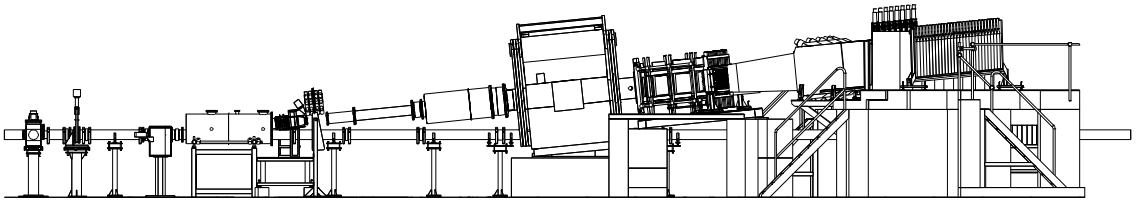

Figure 5.5: *Setup side view.*

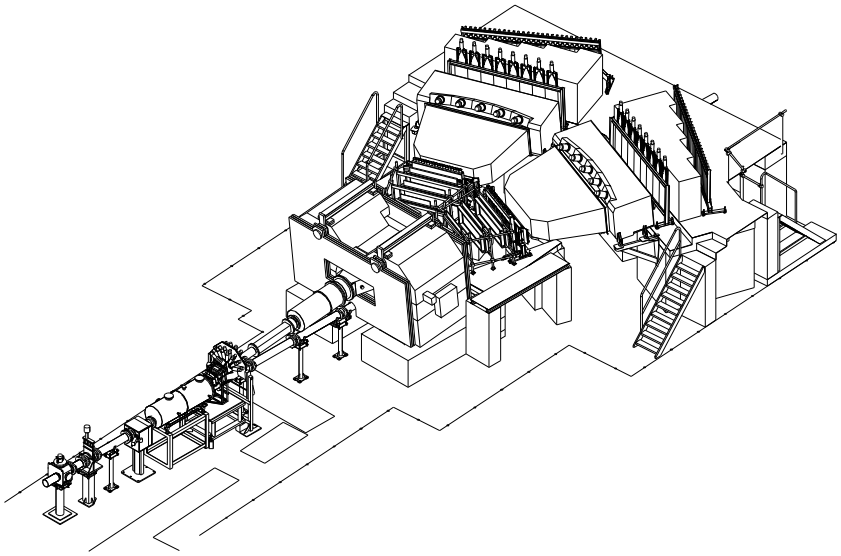

Figure 5.6: *DIRAC setup isometric view. The radiation shielding boundaries are drawn on the floor.*

The Scintillating Fibre Detector

The SFD, made of 0.5 mm diameter scintillating fibres, contains 2 planes (X and Y). Five fibres, forming one sensitive column parallel to z axis, are mapped to one channel of Hamamatsu H6568 16 channel position-sensitive photomultiplier (PSPM). Each plane of size 104 mm by 104 mm contains 240 sensitive columns and is viewed by 15 PSPM's. This counter having a good spatial resolution (127 μm r.m.s) and also a good time resolution (550 ps r.m.s) is used for both triggering and tracking. In the tracking, the counter is used to detect a pair of hits with a relative distance ≤ 9 mm. In the tracking, despite its moderate spatial resolution as a tracking device, this counter was shown to be very useful in reconstructing atomic pairs thanks to its high efficiency, low background, and capacity to tell the hit timing. Through 1999–2000 runs, this counter was proven to possess a very high reliability even in a high beam intensity environment.

The Ionisation Hodoscope

The IH is made of two layers of 16 vertical scintillator slabs (10 cm high, 6 mm wide and 2 mm thick). This detector discriminates at the second trigger level the double ionisation signals expected for close pairs from $A_{2\pi}$.

5.2.2 Detectors downstream of the magnet

The Drift Chambers

The DC system consists of four chamber modules per arm. The first module (DC1) has a frame common to both arms; it has two active regions of 40×80 cm^2 housing 6 planes of signal wires (X, Y, W, X$'$, Y$'$, W$'$). Three modules are then placed on each spectrometer arm:

DC2 with an active area of 40×80 cm^2 and 2 wire planes (X, Y);

DC3 with an active area of 40×112 cm^2 and 2 wire planes (X, Y);

DC4 with an active area 40×128 cm^2 and 4 wire planes (X, Y, X$'$, Y$'$).

The drift cell layout, common to all chambers, consists of a sensitive region around the anode wire (copper-beryllium 50 μm diameter) of 1×1 cm^2 limited by cathode planes (carbon-coated Mylar foils 20 μm thick) and potential wires (copper-beryllium 100 μm diameter).

The chambers are operated with an $\mathrm{Ar}(50\%) + \mathrm{iC_4H_{10}}(50\%) + \mathrm{H_2O}(0.5\%)$ gas mixture and the anode wire HV is 3.8 kV.

The DC single hit resolution is ~ 80 μm. The efficiency of each chamber is around 97% which corresponds to a reconstruction efficiency on one track of 99% (one does not request, that all planes give a hit). The signals of the DC hit wires are also used to implement the fourth level topological trigger, which selects track pairs with small relative momentum.

The Vertical Hodoscopes

Each VH covers an area of 40×130 cm^2 with an array of 18 scintillator slabs (40 cm high, 7 cm wide and 2 cm thick) arranged vertically. All the slabs (Bicron BC420) are connected at both ends to photomultipliers by means of fish tail light guides. The photomultipliers (Hamamatsu R1828-01) are equipped with voltage dividers, which allow

to operate the detector at high counting rates. Each slab could work with a particle flux up to 1.2 MHz, with additional HV applied to the last four dynode stages.

These detectors are used to perform fast coincidences between the two arms of the spectrometer at first trigger level, and also to select low Q_L pairs at higher trigger level. The VH efficiency is 99.5% for the positive, and 98.8% for the negative hodoscope arm. Each slab of the VH has an intrinsic time resolution of ~ 127 ps r.m.s. which provides a time resolution of 180 ps on the hit time difference between the two arms. This timing capability allows to separate pions from protons in the momentum range 1–6 GeV/c, and pions from kaons from 1 to 3 GeV/c.

The Horizontal Hodoscopes

The HH are scintillator hodoscopes with horizontal slabs, covering an area of 40×130 cm^2. Each HH consists of 16 elements (130×2.5 cm^2 with a thickness of 2.5 cm) connected at both ends to photomultipliers. Each photomultiplier (Philips XP2008) is equipped, as for VH, with a voltage divider allowing high counting rates.

The HH contribute to the first trigger level by applying a coplanarity cut on track pairs ($\Delta y \leq 7.5$ cm). The efficiency of HH is $> 96.6\%$ (both arms), and the time resolution is 320 ps r.m.s.

The Cherenkov Counters

The two gas Cherenkov counters used for $A_{2\pi}$ studies have a total length of 285 cm. Their entrance windows have dimensions 143×56 cm^2 and the exit ones 336×96 cm^2. The gas radiator employed is N_2 at NTP.

Each counter is provided with 20 mirrors, and 10 photomultipliers on two rows. Cherenkov light reflected by pairs of adjacent mirrors is focused onto the same photomultiplier (Hamamatsu R1587 with UV-glass window). Mirrors are spherically deformed rectangles, with average dimensions 30×35 cm^2 and 6 mm thickness.

Cherenkov signals are used at first trigger level for rejecting e^+e^- pairs. Both counters have an efficiency $> 99.8\%$ and the pion contamination above the detection threshold is less than 1.5%. Such contamination arises from pion with momenta above the Cherenkov threshold and from accidental coincidences occurring within the gate window.

The Preshower Detectors

The PSh detectors consist of 8 elements per arm and cover an area of 280×75 cm^2. Each PSh element consists of a Pb converter and a scintillator counter placed behind it. The first two converter elements (those farthest from the proton beam line) have a thickness of 1 cm, whereas the others have a thickness of 2.5 cm.

The scintillator slabs (Bicron BC408) have lateral dimensions 35×75 cm^2 and thickness 1 cm. EMI 9954-B photomultipliers are connected to the top of each slab by means of light guides. Since the maximal particle flux on each PSh counter is as high as ~ 2 MHz, an additional 800 V supply is connected to the last dynodes of the photomultipliers.

The efficiency of the detector is $\sim 99.5\%$ (both arms). PSh is used mainly to improve the electron rejection power in the offline analysis, and online to construct trigger levels 0 and 1.

The Muon Hodoscopes

Two muon identification systems are located after thick iron absorbers. Each hodoscope is made of two layers of 28 scintillator slabs having the same area (75×12 cm^2), but different thicknesses (0.5 cm on the first layer and 1 or 0.5 cm on the second one). At present, this detector is used to reject muons in the offline analysis. Using of meantimers as coincidence units allow us to obtain good reduction of background together with high time resolution ($\sigma \approx 1$ ns).

5.3 The Trigger

The present scheme of the DIRAC trigger is shown in fig. 5.7. The first trigger level T1 requires coincidences in the two downstream arms of the spectrometer.

Since the pion pairs from the $A_{2\pi}$ atom breakup have small relative momenta Q, the higher trigger levels suppress pairs with large relative momentum. The second trigger level T2 selects pairs in the upstream region, with small distances Δx between the two particles, by using the information of the IH and of the SFD. This limits the Q_x value of the pair.

The third trigger level T3 provides a further suppression of high relative momentum pairs through a cut on Q_L. It uses the hit patterns of the vertical (VH1, VH2) and of the ionisation (IH) hodoscopes.

A neural network trigger (called DNA) fulfils a task close to that of T3, since it has been trained to select low-Q events. The AND/OR combination of T3 and DNA is used to set the "good event" flag. The data readout is started if T4 has asserted the positive decision and the "good event" flag has been set.

The logic of T2, T3 and DNA is started by the pre-trigger T0, which is a simple coincidence among the detectors VH, PSh and IH.

The final trigger T4 provides the strongest cut on Q of the track pair by making use of the drift chamber signals. The T4 processor compares online the DC wire hits with the content of a pre-loaded table, which contains low-Q "good event" patterns.

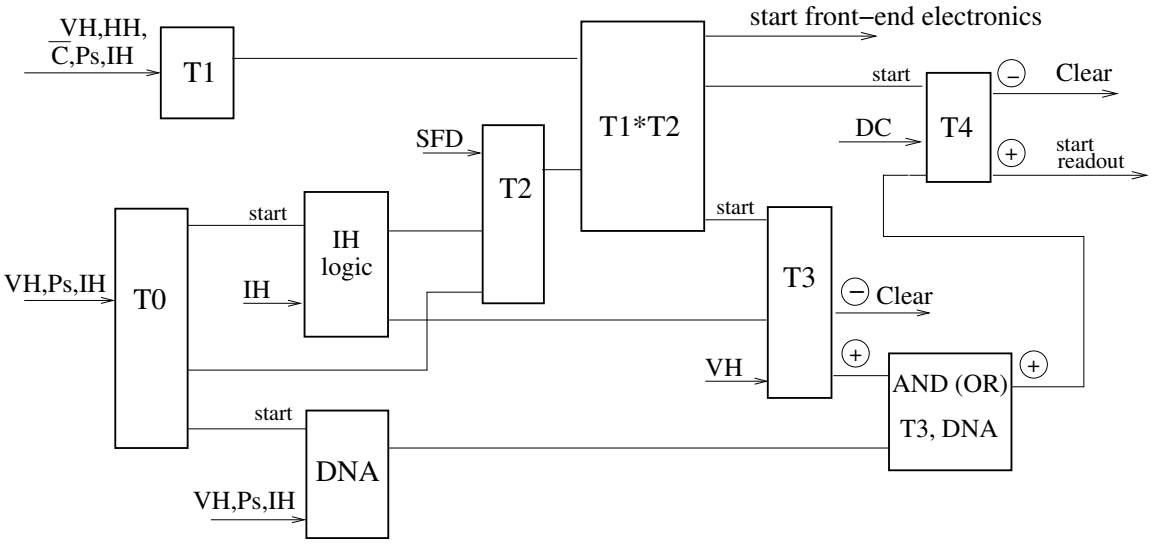

Figure 5.7: *DIRAC trigger scheme.*

5.4 The Data Acquisition System

The detailed scheme of the DIRAC Data AcQuisition system (DAQ) is described in [OLSH00]. The data collected during the PS accelerator burst are transferred to VME memory modules (via the FERA bus) or stored inside other dedicated electronic modules without any software intervention. When data for the current burst are accepted, the DAQ software performs readout as well as event building and transfers events to the central data recorder and on-line monitoring hosts. The custom-made software has been operating since 1998 without any significant changes and has proven to be reliable and simple in use.

At the moment, the DIRAC DAQ is able to accept data from 3 consecutive bursts per PS supercycle, each containing up to 2 MB of data. With the current event size (about 1.2 kB at intensity of 10^{11} p/burst) this implies 1700 events per accelerator burst corresponding to about 5000 events per PS supercycle.

We plan to improve the current DAQ system for future runs in 2001 and 2002. These improvements are described in ref.[OLSH00A] and will include moving the layer of event building from the VME processor board to the main DAQ host and replacing the 10 Mbit Ethernet links currently used by 100 Mbit ones. This will allow us to increase the volume of stored data by a factor 4, and to reduce load and memory requirements of the VME processor. An additional advantage of the new system [OLSH00A] is, that it is more scalable. It allows, if necessary, to use several VME processors (or another data sources) without significant redesign of the DAQ software.

5.5 Data processing and calibration measurements

The offline analysis of the experimental data aims to reconstruct the $\pi\pi$ pairs originating from the break-up of $A_{2\pi}$ atoms. The corresponding kinematics imposes a track separation with an opening angle equivalent to 500 μm spatial separation at 290 cm distance from the target (SFD) and a small relative c.m.s. momentum $Q < 2$ MeV/c.

The program searches for track candidates downstream the magnet, exploiting DC data. At first, only hit wires are used to achieve a fast pattern recognition. Next, fringe field corrections (of the order of 50 μm) are applied, to allow a straight representation. Furthermore, recorded drift times are used to refine the pattern recognition and to solve left/right ambiguities, inherent to such detectors. Eventually one gets an estimation of the 4 track-parameters at the exit of the magnet.

We determined, via prior studies on real data, an approximate lateral beam position, which is run-dependent. In a separate prior work we studied tracks, this time via simulation, from the target in a phase space volume covering our setup and with a mesh, thin enough, to get a final and good precision. The tracks were propagated through the magnetic field, and a few functions were determined, to avoid later lengthy calculations involving the field map for every real track. These functions, polynomial expansions, allow to estimate the track momentum from the 4 track-parameters (see above) and from the assumed track origin at the target for the current run. Other functions allow to calculate the track intersection with upstream planes, given the momentum and again the 4 track-parameters.

For real tracks a standard least-squares fit is made on the DC observations to estimate the 4 track-parameters. A first approximation of the momentum is then obtained (function described above) using the estimated beam position. The usual Kalman-filter method is used to propagate the track information matrix upstream, plane after plane, using the functions above to predict and subsequently select the observed digitizations. Finally a vertex fit is made.

5.5.1 Calibration with Coulomb peak

The reconstruction of Coulomb-correlated $\pi^+\pi^-$ pairs is sensitive to the precision of the setup alignment. Any misalignment of the tracking system in one arm relative to the other arm would generate asymmetrical errors on the reconstructed momenta. This would lead to a systematic shift and additional spread of the Coulomb peak in the Q_L distribution (see fig. 5.8). The mean value of the Coulomb peak is close to zero, well within the accepted tolerances.

5.5.2 Calibration with particle decays

It was proposed [ADEV95] to use the $\Lambda \to p\pi^-$ decay for the telescope position tuning. The Λ mass reconstruction is presented in fig. 5.9. The effective mass distribution has been fitted by the sum of a Gaussian and a polynomial distribution. The Gaussian has a standard deviation $\sigma_\Lambda = 0.43$ MeV/c^2: this value is better than in the experiment by Hartouni [HART94], where the most precise measurement of M_Λ with the standard deviation $\sigma_\Lambda = 0.49$ MeV/c^2 was performed. Our measured peak position is 1115.93 MeV/c^2 with the statistical error ± 0.01 MeV/c^2. Compared to the standard value of M_Λ, one concludes that our result is slightly shifted to higher mass. This shift means that the real telescope position is rotated by a small angle compared to the measured position. The analysis of the effective mass distribution with the Λ decay peak gives the possibility to correct angular distortions of the telescope position.

5.5.3 Calibration with e^+e^- pairs

Accurate time measurement is a crucial point for DIRAC data analysis. Precise timing information is provided by the VH described in section 5.2.2. Time measurements calibration is performed, in the present DIRAC setup, using the data sample collected with the T1 electron-positron trigger. This trigger selects mainly e^+e^- pairs from γ conversions which are almost synchronous in time, as the time of flight for e^+e^- pair does not depend on the momentum in the region of the setup acceptance. In addition, they can be strictly selected with Cherenkov counters. Therefore the e^+e^- pair distribution as a function of time difference between positive and negative arms of the hodoscopes contains only one peak of real coincidence (see fig. 5.10a).

5.5.4 Mass identification of time correlated pairs

Vertical Hodoscope is also used to identify $K^+\pi^-$ and $p^+\pi^-$ pairs which contaminate time correlated $\pi^+\pi^-$ pairs. The distribution of the time difference of the hits in the positive and negative arms is shown in fig. 5.10b for hadron pairs collected with the main

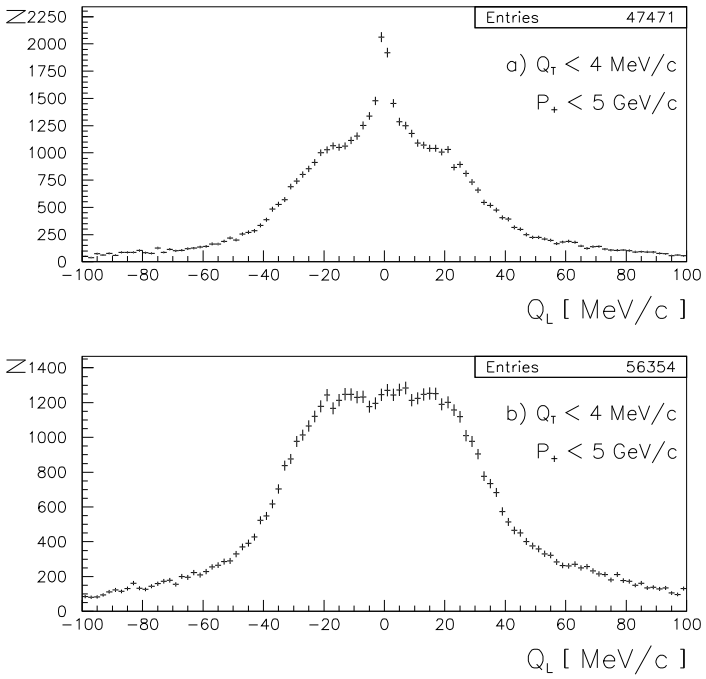

Figure 5.8: *The event distribution of Q_L a) for "real" and "accidental" pairs; b) for pure "accidental" pairs.*

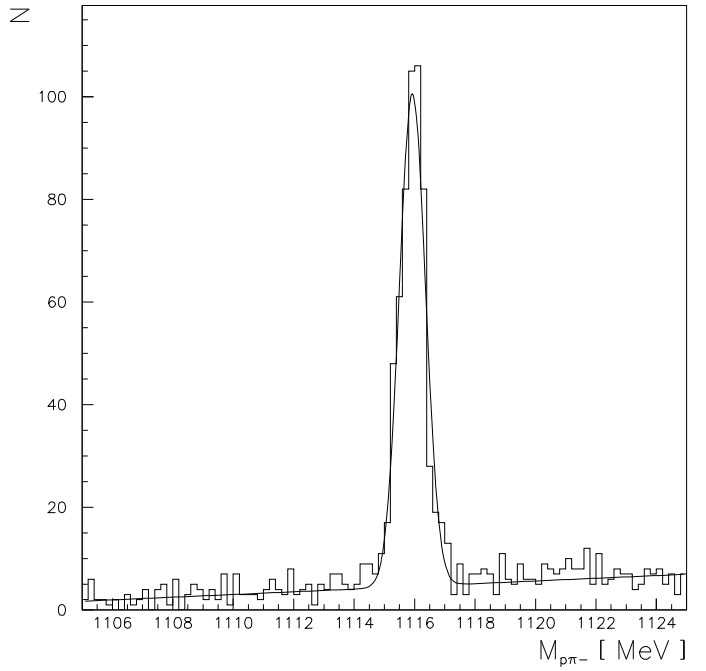

Figure 5.9: *Effective mass distribution for $p\pi^-$ pairs coming from Λ decay at $4.7 < p_\Lambda < 6.5$ GeV/c.*

DIRAC trigger. Here, one can observe the peak of time correlated particles over the flat plateau of accidental coincidences. The peak is asymmetric, the right side excess is due to the presence of slower protons and kaons hitting the positive arm. The plateau, on both sides of the peak, provides the data sample of accidental pairs needed for the analysis.

To identify $\pi^+\pi^-$, $K^+\pi^-$ and $p^+\pi^-$ pairs we can measure the time-of-flight difference between negative and positive particles coming from the target. Assuming the negative particle to be π^- we can reconstruct the mass of the positive particle. The squared mass spectrum of positive particles is shown in fig. 5.10c. Three peaks can be identified corresponding to π^+, K^+ and p^+ particles correlated to the π^-.

5.5.5 Setup momentum resolution

The setup resolutions of projections of the relative momentum of $\pi^+\pi^-$ pairs are shown in table 5.1. The setup resolution is comparable with the relative momentum distribution of "atomic pairs" (see section 4.3). The high relative momentum resolution on the relative momentum gives us the possibility to detect pairs from $A_{2\pi}$ breakup, which are characterised by low relative momentum in their centre of mass system ($Q < 2$ MeV/c).

Table 5.1: *Setup resolution of projections of the relative $\pi^+\pi^-$ momentum in pair c.m.s.*

Detector	SFD	SFD+MSGC(X, X′)	SFD+MSGC(Y, X or X′)
σ_{Q_x}, MeV/c	0.5	0.2	0.3
σ_{Q_y}, MeV/c	0.5	0.4	0.3
σ_{Q_L}, MeV/c	0.6	0.6	0.6

5.6 Experimental conditions

The present experimental conditions in the DIRAC run of 2000 are reported in table 5.2. Here, the counting rate information for each trigger detector is shown at beam intensity of $\sim 0.9 \cdot 10^{11}$ protons per spill ($t_{spill} \approx 0.4$ s). The initial 14 kHz rate of T1 trigger is reduced by the higher level triggers: T2 with a rejection factor 1.4, T3 or DNA with a rejection factor 2 and the first stage of T4 with a rejection factor 1.2 (all rejection factors are with respect to T1). This enables us to collect around 1750 triggers per spill in the actual experimental conditions with mixed trigger (pion trigger including T3, DNA and T4, plus additional 10% of T1 electron trigger and 10% of Λ triggers). Table 5.3 shows the average occupancy in upstream (MSGCs and SFD) and downstream (DC) detectors. The percentage of different event topologies for the reconstructed events is presented in table 5.4 with respect to the total number of recorded events..

Using the $\pi^+\pi^-$ data sample collected with the standard DIRAC trigger, it is possible to estimate, in an approximate way, the number of detected "atomic pairs". For this estimate we have considered only events with 1 reconstructed track in each arm (1×1) and among them we have selected those in which each track has a corresponding hit in the SFD ("good-pair" $\pi^+\pi^-$ events). The percentage of reconstructed "1×1-track good-pair" events for different time intervals and momentum ranges is shown in table 5.5.

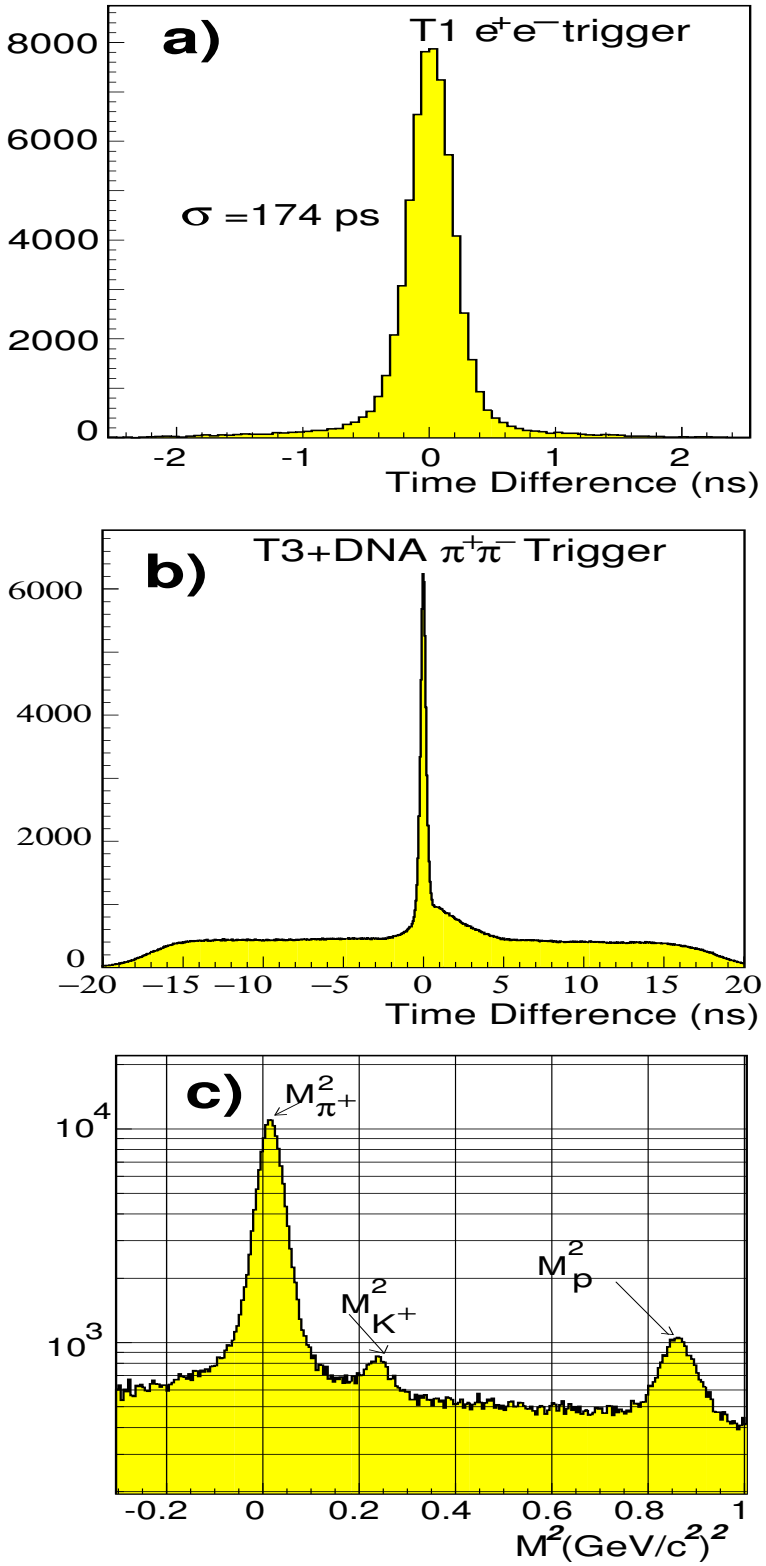

Figure 5.10: *a) VH time difference spectrum for electron-positron T1 trigger. b) Time difference spectrum from events collected with the standard DIRAC trigger. c) Mass spectrum of positive particles recorded with the standard DIRAC trigger.*

Table 5.2: *Counting rate and multiplicity for triggering detectors at an average intensity* $I_P = 0.9 \cdot 10^{11}$ *protons/spill* ($t_{spill} \approx 0.4$ *s).*

Detectors	Counts per spill, 10^3	Counts per second, 10^3	Counts max. per channel & spill, 10^3	Counts max. per channel & second, 10^3	Average multiplicity per event
IH A	2290	5090	143	318	3.36
IH B	1990	4420	124	276	3.35
VH left	790	1760	83	184	1.20
VH right	530	1170	44	98	1.28
HH left	720	1600	70	156	1.28
HH right	500	1110	43	96	1.36
PSh left	790	1750	176	391	1.26
PSh right	540	1190	113	251	1.32
Mu left	84	187	3	7	0.114
Mu right	57	127	2	5	0.097

Table 5.3: *Average occupancy in tracking detectors.*

MSGC average clusters per event	SFD average hit columns per event	DC1 average hit wires per event	DC2 average hit wires per event	DC3 average hit wires per event	DC4 average hit wires per event
15.3	3.34	6.28	6.16	5.42	5.97

Table 5.4: *Percentage of different event topologies with respect to the total number of recorded events.*

"1 × 1-track" events %	"1 × 1-good-pair" events	"1 × 2-track" events %	"2 × 1-track" events %	"2 × 2-track" events %
69.71 ± 0.02	32.88 ± 0.02	4.273 ± 0.008	2.194 ± 0.003	0.132 ± 0.002

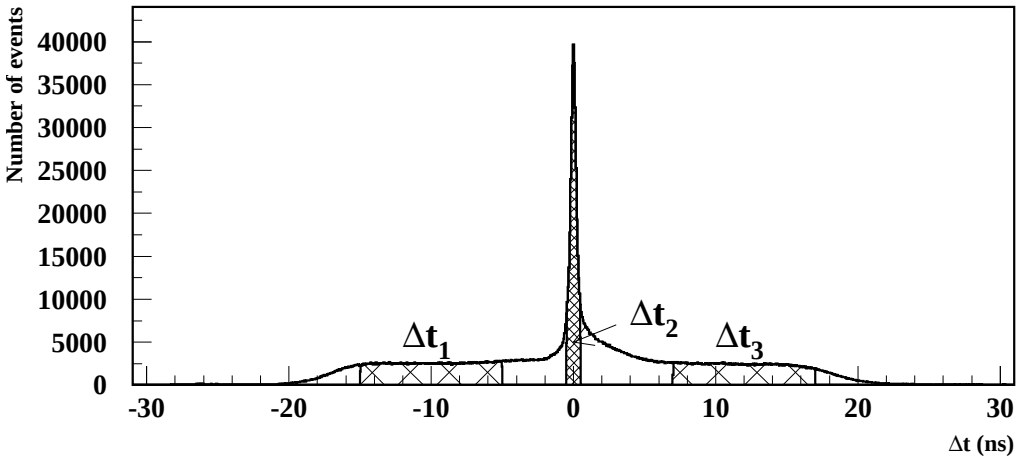

Figure 5.11: *Time difference between hits in VH placed on the two arms.*

We have used the spectrum in fig. 5.11, which shows the time difference between hits in the VH arms, to define the following time intervals: $-15.0 < \Delta t_1 < -5.0$ ns and $7.0 < \Delta t_3 < 17.0$ ns in order to estimate the number of accidental pairs in the peak region: $-0.5 < \Delta t_2 < 0.5$ ns (N_{acc}^{peak}). Hence we select a sample of time correlated pairs ("real coincidence" $N_{\rm real}$).

As shown in table 5.5, the rate of correlated $\pi^+\pi^-$ pairs ($N_{\rm real}$) with $|Q| < 2$ MeV/c is at present ~ 15 per million of collected $\pi^+\pi^-$ triggers. Among the correlated $\pi^+\pi^-$ pairs we expect a contribution of ~ 3 coming from "atomic pairs".

Table 5.5: *Percentage of reconstructed "*1×1 *good-pair" events for different relative momentum regions and time intervals with respect to* $\pi^+\pi^-$ *triggers*

Number "good-pair" events(%)	"1×1-track" events	"1×1-track" events $Q_l < 30$ MeV/c	"1×1-track" events $Q_L < 30$ MeV/c $Q_x, Q_y < 3$ MeV/c	"1×1-track" events $\lvert Q\rvert < 2$ MeV/c
All	38.39 ± 0.02	18.30 ± 0.02	$(24.8 \pm 0.2)\,10^{-2}$	$(4.2 \pm 0.3)\,10^{-3}$
$\Delta t_1 + \Delta t_3$	15.30 ± 0.02	7.287 ± 0.011	$(9.42 \pm 0.13)\,10^{-2}$	$(1.2 \pm 0.2)\,10^{-3}$
Δt_2	6.739 ± 0.011	3.399 ± 0.008	$(5.69 \pm 0.10)\,10^{-2}$	$(1.5 \pm 0.2)\,10^{-3}$
N_{acc}^{peak}	0.765 ± 0.004	0.364 ± 0.003	$(0.47 \pm 0.03)\,10^{-2}$	$(6.0 \pm 3.4)\,10^{-5}$
N_{real}	5.970 ± 0.010	3.034 ± 0.008	$(5.22 \pm 0.10)\,10^{-2}$	$(1.47 \pm 0.17)\,10^{-3}$

5.7 Preliminary results

In this section we present a preliminary analysis of data, which were collected with a platinum target in November 1999. The data have been processed by means of the offline program described in section 5.5. As mentioned in section 4.3, "atomic pairs" have low relative momentum Q in the centre of mass system ($Q < 3$ MeV/c for $\pi^+\pi^-$ atoms). The distributions of "atomic pair" relative momentum and of its projections are defined by the initial Q distribution of the pairs after breakup, the setup momentum resolution (affects mainly Q_L), the resolution of the pair opening angle measurement and by multiple scattering in target, membranes and detectors (affects mainly Q_T). As a result of the analysis the Q_L distribution for "atomic pairs" is found to show a Gaussian-like shape with $\sigma_{Q_L} = 0.65$ MeV/c. For Q_X and Q_Y the distributions exhibit a value of around 1 MeV/c for both σ_{Q_X} and σ_{Q_Y}. Therefore, a new variable F instead of Q is introduced in order to provide a better signal-to-background ratio:

$$F = \sqrt{\left(\frac{Q_L}{\sigma_{Q_L}}\right)^2 + \left(\frac{Q_X}{\sigma_{Q_X}}\right)^2 + \left(\frac{Q_Y}{\sigma_{Q_Y}}\right)^2}. \tag{5.1}$$

For the analysis events have been preselected applying the following criteria: absence of a signal in the Cherenkov counters; region for the sum of particle momenta in laboratory system: $3 < P_+ + P_- < 9$ GeV/c; region for relative momentum projections: $|Q_L| < 22$ MeV/c, $|Q_X| < 4$ MeV/c, $|Q_Y| < 4$ MeV/c. These selection criteria provide identical efficiency for pairs generated in one proton-target interaction ("real" pairs) and for pairs generated in different proton-target interactions ("accidental" pairs). "Real" and "accidental" pairs are separated using the time difference measured by the vertical hodoscopes (see section 5.5.2).

The distributions of F (5.1) are presented in figure 5.12a for "real" and "accidental" pairs (interval Δt_2 in fig. 5.11), in figure 5.12b for pure "accidental" pairs (intervals Δt_1 and Δt_3 in figure 5.11) and in figure 5.12c for pure "real" pairs. The last distribution has been obtained by subtracting the distribution in fig. 5.12b, multiplied by the factor $\Delta t_2/(\Delta t_1 + \Delta t_3)$ (fig. 5.11), from the distribution in fig. 5.12a.

The distribution of "reals", $dN_{\rm real}/dF$, consists of the sum of three distributions: "atomic pairs" dn_A/dF ($F < 4$ only), "Coulomb" pairs $dN_{\rm real}^{\rm short}/dF$ and "non-Coulomb" pairs $dN_{\rm real}^{\rm long}/dF$ (see chapter 3). In the region $F > 4$ the distribution $dN_{\rm real}/dF$ has been fitted by an approximation function $A(F)$, based on "accidental" pairs. Details about this approximation function (sum of simulated distributions of "Coulomb" and "non-Coulomb" pairs) are described in ref.[AFAN93, ADEV95]. For the fit it is more convenient to use correlation functions, which are defined as the ratio of the "real" distribution $dN_{\rm real}/dF$ (or "free" pair distribution, described by the approximation function $A(F)$) to the "accidental" distribution. In fig. 5.13b the correlation functions of simulated "Coulomb" and "non-Coulomb" pairs are shown as solid and dashed lines, correspondingly. The sum of these two correlation functions with two free parameters (normalisation and fraction of "non-Coulomb" pairs, see chapter 3) are used to fit the experimental correlation function in the interval $F > 4$. Using the parameters obtained from the fit, the fitted function can be extrapolated into the interval $F < 4$. In fig. 5.13a the experimental correlation function, divided by the normalisation factor, is shown with error bars together with the fitted correlation function as smooth curve. In the interval

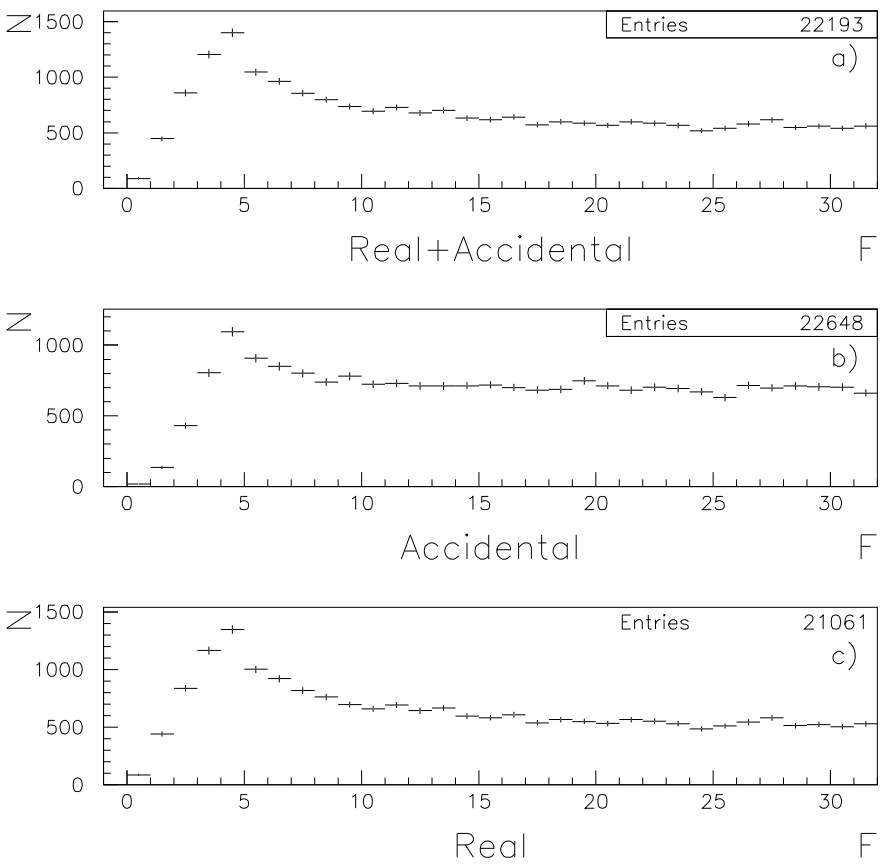

Figure 5.12: The event distributions of F for the mixture of "real" and "accidental" pairs (a), for pure "accidental" pairs (b) and for pure "real" pairs (c).

$F < 4$, where "atomic pairs" are expected, the experimental distribution shows a clear excess of pair events, compared to the fitted correlation function.

The difference between the experimental distribution dN_{real}/dF and $A(F)$ is presented in fig. 5.14. The excess of low-F pairs amounts to:

$$N_{F<2} = 160 \pm 45, \tag{5.2}$$

$$N_{F<3} = 266 \pm 79. \tag{5.3}$$

This excess is compatible with the expected number of "atomic pairs" $n_A \approx 240$.

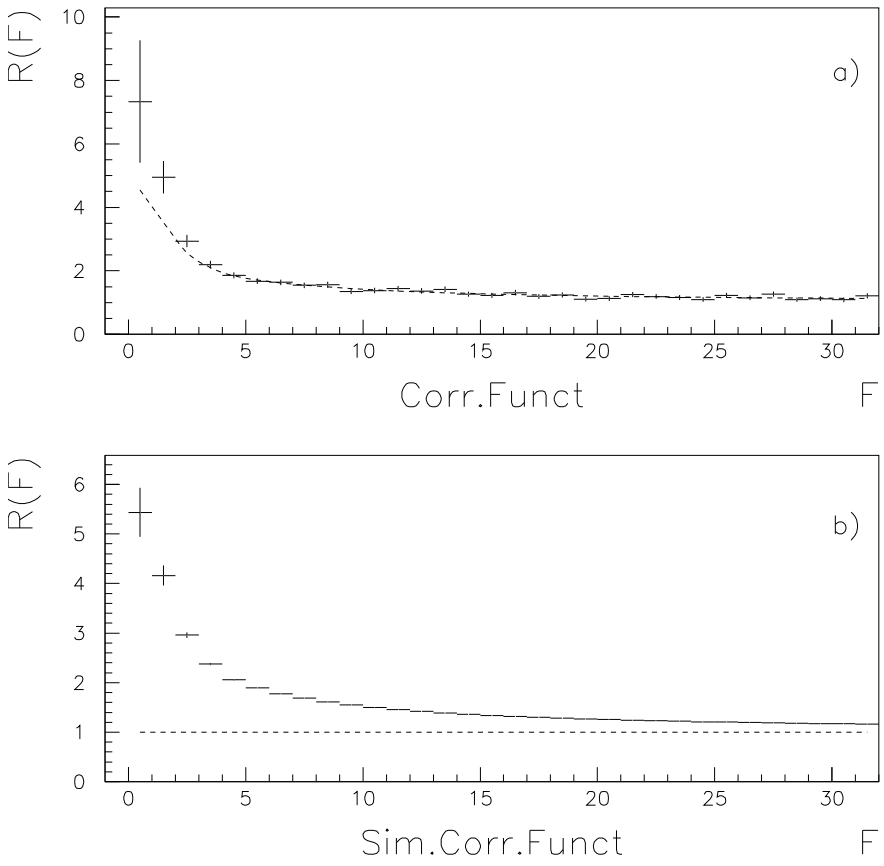

Figure 5.13: a) The experimental correlation function is shown with error bars, and the fitted correlation function is presented by the dashed smooth curve. Both are divided by the normalisation factor of fitted function. The fit has been performed in the interval $F > 4$. b) The correlation functions of simulated "Coulomb" (solid line) and "non-Coulomb" (dashed line) pairs are shown. The sum of these functions, with two free parameters, is used as the correlation function to be fitted.

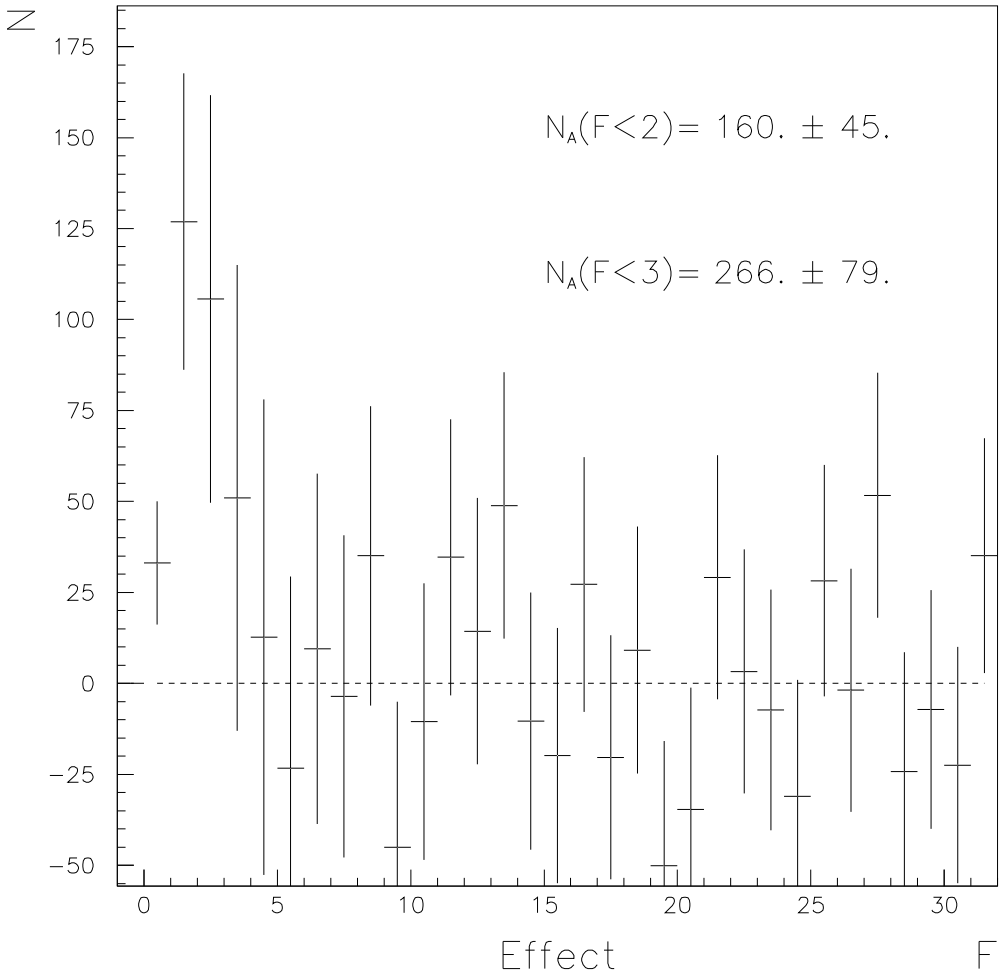

Figure 5.14: The difference between the experimental distribution dN_{real}/dF and the approximation function $A(F)$, describing the contribution of pairs from free states.

Chapter 6

Modifications of the DIRAC setup for $A_{\pi K}$ detection

The present DIRAC setup is dedicated to the detection of $\pi^+\pi^-$ pairs with small relative momenta. Two identical arms are located symmetrically to the secondary particle beam. Contrary to $\pi\pi$ pairs π and K pairs from $A_{\pi^+K^-}$ and $A_{K^+\pi^-}$ breakup have momenta, that differ by a factor 3.5. Hence, in principle, the position of the detectors with respect to the secondary particle beam should be changed to optimise the setup acceptance for such pairs.

Meanwhile simulations showed, that both types of atoms can be detected in the present setup geometry with acceptable efficiency, if we implement additional Cherenkov counters to separate pions, kaons and protons.

Therefore, the experiment for $A_{\pi K}$ studies will be performed in two steps. First, only new Cherenkov counters will be added without changing the setup geometry. Second, the secondary particle channel as well as the detectors will be rotated in the median plane of the channel and the detectors in order to optimise the setup position for detection of either $A_{\pi^+K^-}$ or $A_{K^+\pi^-}$. The decision, which kind of atoms should be searched for in the second step, will depend on results, obtained during the first step of the experiment.

For both steps we plan to improve the trigger and the tracking. For this purpose we will install additional planes of scintillating fibres: a U-plane close to the existing two SFD planes (X and Y) and one X-plane in the fringe field of the spectrometer magnet. This will improve the identification of two particles, hitting only one fibre in the existing SFD.

In addition, we plan to implement in the upstream setup region one among the following detectors:

— Triple GEM detector — a multistep gas avalanche detector, that exhibits a high rate capability with a time resolution below 10 ns;

— Silicon microstrip detector — a reliable detector capable to work at high particle fluxes;

— Micro drift chambers with small gap ($\sim$ 3 mm) — a detector with high coordinate precision.

The detector studies will permit to choose the optimal detector in terms of counting rate, dead time and coordinate resolution.

6.1 Modification of the setup in the present geometry

Before modifying the geometry of the DIRAC setup for a dedicated measurement of the $A_{\pi K}$ lifetime through a detection of either π^+K^- or $K^+\pi^-$ breakup pairs, we have investigated the possibility to detect simultaneously $\pi\pi$ and πK "atomic pairs" using the present setup geometry. This approach might allow us to provide the first evidence of πK "atomic pairs" already in the year 2002, meanwhile accumulating the necessary statistics for the determination of the $A_{2\pi}$ lifetime with the proposed accuracy, and allow us to select the proper channel (π^+K^- *or* π^-K^+) to be investigated in a following step.

The yield of $A_{\pi K}$ in the present DIRAC setup has been described in chapter 2. The corresponding momentum spectrum for π^+K^- pairs is shown in fig. 2.1. The expected yield is low, and only $A_{\pi K}$ with momenta higher than $\sim$ 5.8 GeV/c will breakup into detectable πK pairs, namely pairs entering the apparatus acceptance. The pion of the pair will have a momentum range between 1.25 and 2.3 GeV/c, whereas the kaon will have a momentum between 4.6 GeV/c and the maximum accepted momentum of the setup, namely $\sim$ 7 GeV/c. The topology of such events for π^+K^- is shown in fig. 6.1. The high momentum kaon trajectories are close to the setup symmetry axis, whereas the correlated low momentum pions are away from the axis.

A possible way to detect πK "atomic pairs" in the present setup is to employ additional threshold Cherenkov detectors for pion/kaon (and kaon/proton) discrimination at trigger level. Furthermore, since the present setup has a symmetric geometry we will detect simultaneously πK "atomic pairs" of both sign combinations.

The implementation of new detectors and trigger schemes should, however, not affect the detection efficiency of $\pi^+\pi^-$ atomic pairs, as these class of events will still constitute the bulk of our collected data.

In order to detect π^+K^- "atomic pairs" one needs to discriminate pions from kaons in the negative arm. To this aim we need to place a small-size threshold Cherenkov counter

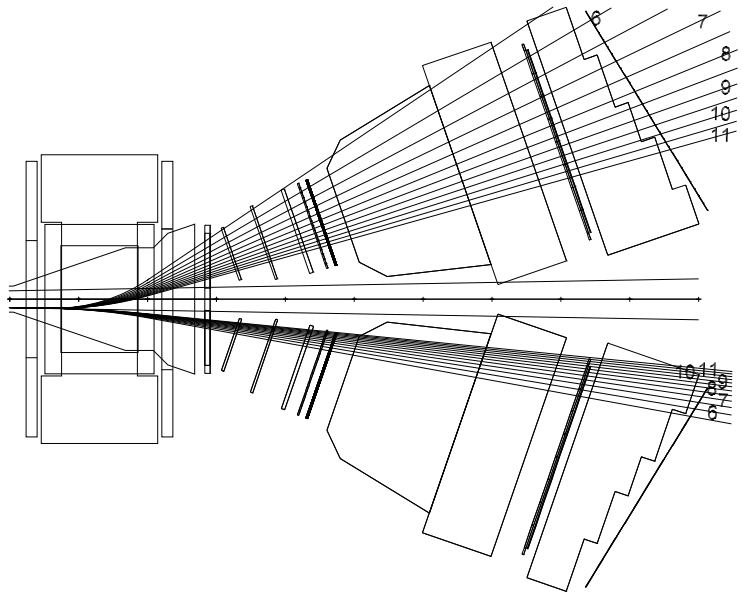

Figure 6.1: *Trajectories of π^+ and K^- from the $A_{\pi^+K^-}$ breakup for the existing setup. The labels on the trajectory lines are the $A_{\pi^+K^-}$ momenta in GeV/c.*

between the Horizontal Hodoscope and the present Cherenkov detector (fig. 6.2). Due to the limited space available, the new counter should extend longitudinally within the volume of the existing counter, and, transversally it should cover only the solid angle of K^- coming from $A_{\pi K}$ breakup ($\sim 4.7^\circ$ in the horizontal plane). The dimensions of the entrance window could be 290×410 mm^2 (width $\times$ height), of the exit window 350×630 mm^2 and the total length of the counter could be ~ 800 mm. The counter will be equipped with two mirrors of the same size as those currently used, namely with dimensions 320×350 mm^2, and two 5-inches photomultipliers of the type Hamamatsu R1587. Some spare mirrors and PMs are already available. We plan to employ Freon 114 at atmospheric pressure as gas radiator because it has a high index of refraction (n=1.0014). This radiator is suitable to discriminate pions from kaons in the kinematic range of accepted $A_{\pi K}$ since their Cherenkov momentum threshold is 2.6 GeV/c and 9.3 GeV/c, respectively. We expect $N_{p.e.} \approx 14$ for 4.5 GeV/c pions. Freon 114 is environmentally safe, non-flammable and can be operated at room temperature, and has a well-understood behaviour from previous experiments.

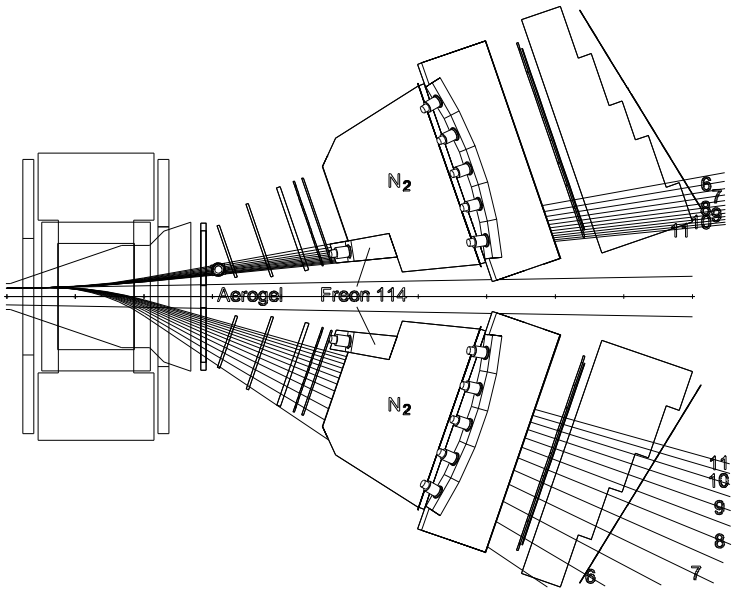

Figure 6.2: *Trajectories of π^- and K^+ from the $A_{K^+\pi^-}$ breakup for the existing geometry with Freon 114 Cherenkov counter and with Silica Aerogel threshold Cherenkov detector. The labels on the trajectory lines are the $A_{K^+\pi^-}$ momenta in GeV/c.*

The selection of negative kaons from other particles at first trigger level will require the coincidence between the negative responses from both N_2 and Freon 114 Cherenkov counters.

The detection of $\pi^- K^+$ pairs is somehow more complex as in this case, in addition to π^+, a large admixture of protons to positive kaons is also expected. The discrimination of π^+ from K^+ can be achieved with a threshold Freon 114 Cherenkov counter identical to the one used in the negative arm. To achieve an efficient kaon/proton discrimination at trigger level, we will install a small Silica Aerogel threshold Cherenkov detector on the positive arm (fig. 6.2). The aerogel detector will be placed between the first (DC1) and second (DC2) drift chamber modules. One module of Silica Aerogel tiles with average dimensions $150 \times 350 \times 200$ mm^2 (width $\times$ height $\times$ length) would be sufficient

to intersect all trajectories of K^+ from $A_{\pi K}$ breakup. The module is viewed by two 5-inches photomultipliers (Hamamatsu R1587) attached to the top and bottom sides. To discriminate between kaons and protons in the kinematical range of $A_{\pi K}$ breakup, aerogel with index of refraction n=1.008 would be the most appropriate. However, extensively tested aerogel tiles only with n=1.01–1.03 are available from the Belle Collaboration at KEK [SUMI99]. With n=1.01 the momentum threshold for protons (6.62 GeV/c) is slightly below the maximum momentum of protons entering the apparatus (7.0 GeV/c). Therefore, some Cherenkov light will be emitted by the fastest protons. However, the intensity of the light will be very weak: in 200 mm thick aerogel radiator one expects an average of 3−4 p.e. from 7.0 GeV/c protons, and about 13−14 p.e. from kaons with 4.6 GeV/c momentum (minimum momentum from $A_{\pi K}$ breakup). Therefore, we still expect a wide separation region which should allow an efficient proton/kaon discrimination when operating the detector in the threshold mode. Additional investigations of the properties of silica aerogel with very low index of refraction (n $<$ 1.01) are currently in progress at JINR Dubna, and we intend to exploit both the Japanese and Russian technologies.

6.2 Modification of the setup geometry

According to our calculations of the $A_{\pi^+K^-}$ and $A_{K^+\pi^-}$ yields in different geometrical configurations of the experimental setup (see chapter 2), it is possible to optimise the setup geometry to maximise the detection of specific type of such atoms. As shown in table 2.1, the geometry which has the maximal yield of *either* $A_{\pi^+K^-}$ *or* $A_{K^+\pi^-}$ consists of a rotation of detectors and of the secondary particles channel by +4.0° and −1.5°, respectively, as shown in fig. 6.3.

The modification procedure of the present DIRAC geometry is described in details in Appendix A.

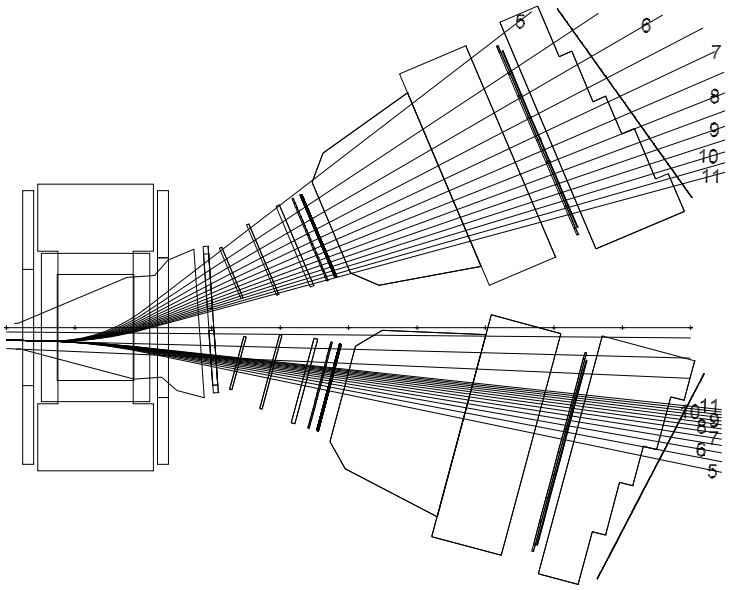

Figure 6.3: *Trajectories of π^+ and K^- from the $A_{\pi^+K^-}$ breakup for the setup with modified geometry. The labels on the trajectory lines are the $A_{\pi^+K^-}$ momenta in GeV/c.*

6.3 Upgrades and new detectors

To study πK atoms it will be necessary to increase the proton beam intensity since the $A_{\pi K}$ yield is lower than that of $A_{2\pi}$. Therefore, it will be necessary to upgrade or replace those detectors which may not withstand the high counting rate. On the other hand, a different trigger scheme should be implemented and better tracking capabilities be investigated. Thus we envisage detector upgrades and replacements.

6.3.1 Triple GEM detector

To cope with a higher particle flux, the present MSGC detector could be replaced with a triple GEM detector (fig. 6.4). The triple GEM is a multistep gas avalanche detector that exhibits a high rate capability with a time resolution below 10 ns. The most promising configuration is that with a 2D (X+Y) charge divider readout (with 200 μm pitch) based on the kapton etching technology [BRES99]. This will allow to detect a track with only two Triple GEM detectors using 2D pulse height correlation. Moreover, the use of a non-flammable and non-aging gas mixture, like Ar-CO_2, will allow to use standard materials for the detector construction. With this mixture, gas gains greater than 10^4 are easily achievable with signal to noise ratios higher than 30. The ionisation gap will have a 3 mm depth and the transfer gaps between GEMs and last collection gap will be around 1 mm. The GEM layout will be a standard 140 μm pitch hexagonal pattern of 50/70 μm (internal/external) diameter holes etched in a 50 μm thick kapton foil. Nevertheless, a careful study of GEM gain uniformity and spark probability should be done in order to provide a stable beam operation of the device (spark probability less than 10^{-10} per crossing particle). A GEM segmentation might also be very useful to prevent discharges and short-circuit of GEM foils. The small size, 10×10 cm^2, of the proposed detector will avoid the need for spacers in the GEM active area, and will facilitate the achievement of a good gain uniformity (with variation $< 10\%$ across the detector).

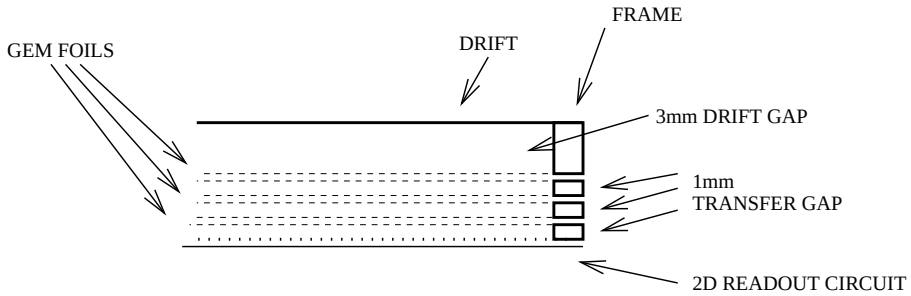

Figure 6.4: *Scheme of the triple GEM detector design.*

Also the electronics used to readout the detector needs to be upgraded, in order to accomplish the following tasks:

— fast signal shaping (time constant below 40 ns);

— high pipeline sampling frequency ($\geq$ 40 MHz);

— fast analogue readout. The total readout time of one detector has to be below 10 μs including digitisation and zero suppression;

— fast clear should be implemented in such a way that last event could be discarded and readout cancelled within few μs;

— data should be stored during the spill in VME standard memories, properly sized to manage more than 6000 triggers.

Such electronics upgrade require a dedicated development based on existing baseline front-end (such as APV [JONE99], Helix [BAUE99], Beetle [BAKE99], etc.).

6.3.2 Silicon Microstrip Detector

Due to the high particle flux present in this region of the DIRAC setup, a solid state tracker seems another very interesting option. The 6-inch technology now available allows the construction of a 10 $\times$ 10 cm^2 detector using a single silicon wafer. A good solution would be a 300 μm thick microstrip silicon detector [BACH99] with a pitch between 100 μm and 200 μm. The existing radiation hard technology allows the use of silicon detectors in extremely irradiated conditions ($>$ 1 Mrad/year in LHC), thus ensuring a long operation ($>$ 10 year) in the less stringent conditions of DIRAC experiment. Considering a typical strip capacitance of 1 pF/cm, in a 10 cm detector with standard electronics (ENC $\sim$ 1800e) a signal to noise ratio of 15, an efficiency around 99% is achievable [CERN00]. A detailed study of the depletion voltage stability considering the DIRAC fluency is important to determine the need of additional detector cooling.

The silicon microstrip detector solution could allow to design a layout close the original MSGC layout consisting of four detector planes with strips at 0°, 90°, 5° and to 85°.

6.3.3 Micro Drift Chambers

The Drift Chamber technique allows for a rigid mechanical design, rather simple production procedures and good features of read-out electronics. These advantageous aspects make the use of Drift Chambers for particle tracking between target and magnet very attractive.. The design of a Micro Drift Chamber with high spatial resolution and with resolving power for nearby tracks is proposed in Appendix B.

6.3.4 SFD upgrade

Based on the fact that SFD is performing quite reliably with a high efficiency in the high intensity beam environment, we envisage an upgrade of SFD in two steps. Often we see candidate events of "atomic pairs" in which, the distance between two hits on SFD is so small that in one of two planes, two hits are recorded only within one column so it looks like a single hit. In this case, it is difficult to produce a good trigger signal, as there are many single-hit events. If we increase the number of planes and make an additional U-plane, we would more flexibility in forming efficient and robust trigger signals. The additional U-plane allows us to make also a tracking with a better spatial resolution than now. Except for the width of the counter which is 15.0 cm, the new plane will be very similar to the existing two planes, thus we are sure to make a well performing plane with our current technique. This is considered to be the step number 1.

Also to separate two close charged particles hitting only one column of X-plane, we plan to make another X-plane SF counter at a large distance from the target at $z = 7.8$ m

as a second step. This plane is placed in the fringe magnetic field of the spectrometer magnet, and even particles having rather high CM momenta can split and hit more than two columns. Thus this will allow us to make an efficient trigger signal even in a very high beam-intensity situation. As the particles coming from the target suffer from multiple scattering in different materials (detectors, windows) the determination of x coordinate with a good resolution just at the entrance of the spectrometer allows us to make a reconstruction of momenta of the particles with small errors. An estimation already done predicts a gain in the momentum resolution with a new plane with a counter resolution of 250 μm even if an additional multiple scattering caused by this plane is taken into account. We plan to make a more detailed simulation in order to establish an optimum trigger logic to be implemented with hardware. A basic study about building a SF plane in vacuum has been already performed at KEK. It was demonstrated that there are no problems in long-term stability either in the tested Kuraray scintillating/clear fiber or in the optical joint. Also a technique to pull out clear fibers through vacuum flanges has been established.

6.3.5 Cherenkov Counters

The Cherenkov detectors upgrade will consist of two steps. The first upgrade is aimed of detecting π^+K^- *and* π^-K^+ pairs with the present DIRAC geometry simultaneously to $A_{2\pi}$ detection. This upgrade has been described in section 6.2. The second upgrade, after completion of $A_{2\pi}$ measurement, is foreseen to optimise the setup geometry for detection of *either* $A_{\pi^+K^-}$ *or* $A_{K^+\pi^-}$, according to the results the first upgrade measurements.

In case of $A_{\pi^+K^-}$ detection, we have to discriminate in the negative arm negative kaons from other particles (electrons, muons and pions). It would be necessary to employ in the existing threshold Cherenkov counter a gas with an index of refraction higher than that of N_2. The required radiator replacement is in principle necessary only for the counter placed on the negative spectrometer arm, maintaining the N_2 gas radiator in the counter on the positive arm, devoted to the selection of positive pions.

For the proposed setup geometry (fig. 6.3) and the accepted $A_{\pi K}$ momentum range (from 5 to 10 GeV/c), the momentum of negative kaons associated to the $A_{\pi K}$ breakup will range between 3.9 and 7.8 GeV/c. Moreover, such kaons will traverse only the central region of the counter. On the opposite arm the correlated positive pions will cover a momentum range from $\sim$ 1.0 to 2.2 GeV/c.

A suitable radiator choice for the Cherenkov counter on the negative arm is sulfur hexafluoride (SF_6) gas, which has an index of refraction n=1.00072 and corresponding threshold on pion and kaon momenta at $\sim$ 3.7 GeV/c and $\sim$ 13.0 GeV/c, respectively. It allows to discriminate pions (muons and electrons) from kaons because only the former will produce Cherenkov light in the appropriate momentum range (3.9$\div$7.8 GeV/c). Pions and kaons with momenta below the Cherenkov threshold and outside the interval of momenta of typical $A_{\pi K}$ breakup products, namely $p_\pi <$ 3.7 GeV/c and 7.8$< p_K <$13 GeV/c, will, however, enter the counter acceptance and contribute to the trigger yield when operating the counter in anticoincidence. The trajectories of such particles will intersect the mirrors located at both extremes of the counter exit window. To reject such a background we propose to reduce the trigger acceptance of the negative arm by excluding the response of photomultipliers located at the edges of the counter.

SF_6 is known to have excellent transparency to light with wavelength above 190 nm [GARW71], comparable to that of N_2, and a scintillation intensity 6.6 times less than in nitrogen [HEIN76], it is inert and non-flammable, and can be operated at NTP. The maximum Cherenkov emission angle is 2.17° to be compared with 1.39° for N_2. Since the optics of the counter is optimised to focus light emitted at a maximum Cherenkov angle of 1.4° we expect a partial loss of Cherenkov photons falling outside the mirror acceptance. This loss does, however, correspond to a negligible loss of efficiency since the expected light yield in SF_6 is larger than in N_2, for the same radiator path length.

We have performed a simulation of the detector response to pions with momenta from 3.9 to 7.8 GeV/c traversing the $\sim$ 2.8 m long SF_6 gas radiator. With the present optical arrangement of the mirrors and photomultipliers, and with a detection threshold set at 5 p.e., the pion detection efficiency is 99.3%, to be compared to a positron detection efficiency of 99.6% for the counter on the positive arm filled with N_2 gas.

An additional option is to operate both counters with an SF_6 gas since all positive pions, including those from $A_{\pi K}$ breakup, have momenta below the Cherenkov threshold. This ensures a light yield higher than with N_2, which should compensate for the partial loss of photons emitted at large Cherenkov angles, and allows a simpler operation of the gas supply system.

In case we choose $A_{K^+\pi^-}$ detection, we need to discriminate K^+ from π^+ and p in the positive arm. The π/K discrimination can be achieved with the same Cherenkov counter filled with SF_6 gas as in the $A_{\pi^+K^-}$ case. To discriminate kaons from protons an aerogel threshold Cherenkov counter with n=1.01 can be used.

In order to investigate in detail the properties of SF_6 gas, we will expose a prototype threshold Cherenkov counter filled with SF_6 to a π/K-test beam. The prototype counter has been previously used to exploit several options for the geometry of the final DIRAC detectors, to investigate two different choices for the radiator (air or nitrogen), to compare the performances of different PM, and to evaluate the counter detection efficiency and the mean number of photoelectrons. A detailed description of the prototype detector geometry and the results obtained from its operation on a test beam, are available in [BRAG99]. The prototype detector is presently at CERN and can be made operational in a short time. We plan also to perform test-beam studies for the Freon 114 and the aerogel (n=1.01) threshold Cherenkov counters.

6.3.6 A permanent magnet near the target

In the present DIRAC setup we have difficulties to measure the opening angle of two tracks that hit the same fibre of the SFD. A way to overcome this problem could be the installation of a permanent magnet close to the target. A permanent magnet with B·L = 0.01 T·m (1000 Gauss for a length of 10 cm) placed near the target will deviate secondary particles with a 3 GeV/c momentum by 1 mm at 1 m. A possible location for the permanent magnet is shown in fig. 6.5. The aperture of the magnet, 60 × 80 mm^2 (height × width), has been chosen on the basis of our knowledge of the proton beam halo dimensions.

Nevertheless, if a second SFD were installed, the most suitable location for this permanent magnet would be at 0.5 m downstream the target. In this way the proton beam would pass under the magnet and the needed magnet aperture would be only 25 × 35 mm^2 (fig. 6.6).

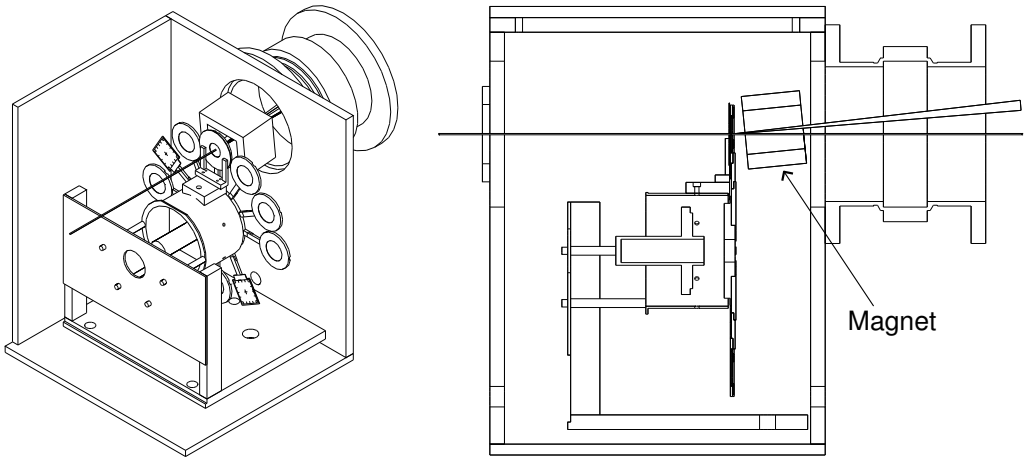

Figure 6.5: *Isometric and side views of the target station with the insertion of a permanent magnet. The proton beam and secondary particle beam are also shown.*

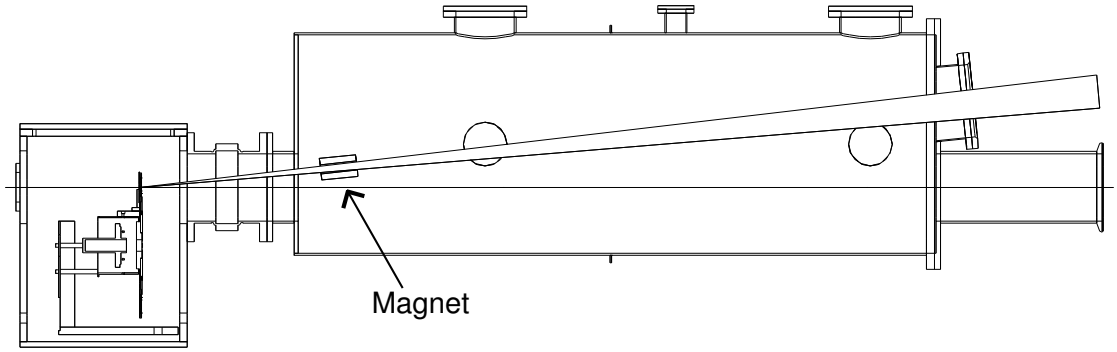

Figure 6.6: *Side view of the target region with a permanent magnet placed in the secondary particle channel at a distance of 0.5 m from the target.*

6.3.7 Trigger, online and offline software

For the study of $A_{\pi^+K^-}$ and $A_{K^+\pi^-}$ atoms both the trigger and the DAQ systems will keep the same structure as the one they have presently. Only minor modifications will be introduced in order to take into account the differences between πK pairs and $\pi^+\pi^-$ pairs.

The logic of T1 trigger level will remain the same even if the negative arm Cherenkov counter will detect also kaons. By using Cherenkov counter signals in anticoincidence, as it is done now, we will suppress positrons on the positive arm, and pions on the negative one. On the other hand, we plan to modify the hardware implementation of T1 by using only universal logic modules (LeCroy 2366). This will improve the flexibility and the reliability of the trigger scheme by reducing the cable interconnections.

The T3 trigger level will be upgraded in order to select π^+K^- and π^-K^+ candidates with a small relative momentum. In fact, it will be necessary to implement a new logic according to the new correlation maps among the VH slabs due to the new event topology and to the rotation of the two spectrometer arms. Any further information coming from new or upgraded upstream detectors could be easily included in the trigger logic.

For the DNA trigger a new training of the neuronal network will be necessary in order

to select π^+K^- and π^-K^+ candidates. This can be done using Monte Carlo data and real data collected with T1 trigger. Furthermore, studies on DNA trigger are in progress in order to implement a network setup able to use also the information of SFD which has a better spatial resolution. Moreover, with a new front-end interface, the correlations between IH and SFD could be established. Finally, we are studying the feasibility of sharpening the coplanarity trigger cut, by using the neural network methods. This will add a stronger constraint on the vertical component of the relative momentum of the pairs.

For the T4 processor, the look-up tables of the track analyser will be modified to take into account the specific track correlations for the πK pairs.

For what concerns online software (DAQ) we don't plan any particular modification. As discussed in the previous chapter, the present DAQ architecture will be able to manage the volume of data foreseen for the new experiment.

Concerning the data processing and the calibration measurements, the same programs we are currently using for analysing $\pi^+\pi^-$ pairs will be used to analyse πK events.

Chapter 7

Other physics subjects

The DIRAC setup may also be used to study other physics topics. Some could be investigated simultaneously with $A_{\pi K}$ observation, and others need minor setup modifications.

7.1 Observation of $A_{2\pi}$ long-lived states

Strong interaction and vacuum polarisation lead to a splitting of $A_{2\pi}$ energy levels and hence to a difference $\Delta E_{\mathrm{ns-np}}$ between ns and np energy levels. For n = 2 the value $\Delta E^{s}_{\mathrm{2s-2p}}$, resulting from strong interaction, is proportional to $(2a_0 + a_2)$ and amounts to

$$\Delta E^{s}_{\mathrm{2s-2p}} \approx -0.3 \text{ eV}. \tag{7.1}$$

The contribution from vacuum polarisation to $\Delta E_{\mathrm{2s-2p}}$ is only [EFIM86]

$$\Delta E^{pol}_{\mathrm{2s-2p}} \approx -0.06 \text{ eV}. \tag{7.2}$$

The simultaneous measurement of the $A_{2\pi}$ lifetime and the Lamb shift allows to obtain a_0 as well as a_2 in a model-independent way.

In order to measure $\Delta E_{\mathrm{ns-np}}$, the dependence of the lifetime for long-lived $A_{2\pi}$ states ($l > 0$) on the applied electric field can be studied [NEME85]. Calculations show that up to $\sim 10\%$ of the atoms, generated in the thin target, reach the vacuum region as long-lived states [AFAN97A]. Such $A_{2\pi}$ atoms may be observed in the DIRAC setup without any change, and the results could demonstrate the feasibility of $\Delta E_{\mathrm{ns-np}}$ measurement.

7.2 Study of charged particle production dynamics using Coulomb correlation

The study of the $\pi^+\pi^-$ Coulomb correlation enables to measure the fractions of pion pairs generated by short-lived (ρ, ω, $\Delta\ldots$) or by long-lived sources (η, $\eta\prime\ldots$) [AFAN91, AFAN97A]. This relation can be measured as a function of the pair energy in the lab system at the few percent level. The identification of K^-, K^+ and p allows to perform the same analysis for further combinations of charged particles. The Coulomb correlations for K^+K^- and K^-p are sensitive to the size of their production region. Therefore the correlation study allows to obtain a picture of this particle production dynamics in coordinate space for light and heavy nuclei.

7.3 Bose-Einstein correlations

A study of the Bose-Einstein correlations in $\pi^-\pi^-$ and $\pi^+\pi^+$ requires the consideration of Coulomb corrections for those pairs, which originate from short-lived sources [LEDN82]. Exploiting the high relative momentum resolution of our spectrometer, it should be possible to extract these corrections from the measurements ($\pi^-\pi^-$, $\pi^+\pi^+$ and $\pi^+\pi^-$) themselves. The data for like-sign particles are taken as a by-product during normal data acquisition.

Chapter 8

Cost estimation and time scale for $A_{\pi K}$ experiment

8.1 Cost estimation

MSGC upgrade

Mother board (10 units)	10.5 kCHF
Hybrids (10 units)	15.5 kCHF
Front-end production	10.5 kCHF
Controller modules (4 + 2 spares)	40 kCHF
VME memories (4 + 2 spares)	47 kCHF
Total sum	123.5 kCHF

Double-sided silicon microstrip detector

Si wafer (double-sided x-y)	15 kCHF	size 100×100
100 μm pitch, 1000 chan. each		
Upilex fanout	10 kCHF	
Va32_75 preamp. (1 plane)	8 kCHF	32+32 chips, 32 channels
Va32_75 probe testing (1 plane) optional	8.5 kCHF	each: 1000(x)+1000(y)
Electronics from Va32_75 to VME (1 plane)	4 kCHF	
Sequencer (1)	5 kCHF	
VME FADC (1)	5.8 kCHF	
CPU VME (1)	9.2 kCHF	
VME crate (1)	11 kCHF	
Power supply (1 module)	5 kCHF	
Mechanics 1 plane (2 planes)	2.5 (7) kCHF	
Cabling and cooling (1 plane)	1.5 kCHF	
Total for 1 plane (opt. with probe testing)	77 (85.5) kCHF)	
Total for 2 planes (opt. with probe testing)	130.8 (147.8) kCHF)	

SFD upgrade

Characteristics of the detectors	step 1 adding U-plane to the existing SFD	step 2 new X-plane to be placed in the fringe field
Number of planes	1 (U)	1 (X)
Position z	3.2 m	7.8 m
Size of the plane	150×150	$333(X) \times 300(Y)$
Fibre diameter	0.5 mm	0.5 mm
Number of columns	340	768/2
Readout columns for track.	340	384
Corresponding resolution	0.127 mm	0.254 mm
Readout columns for trig.	170	384
corresponding resolution	0.254 mm	0.254 mm
Number of PSPM	22	24

SFD cost estimation

Scintillating fiber	1.5 km: 6 kCHF	1.6 km: 7 kCHF
Clear fiber	10 km: 20 kCHF	2.4 km: 5 kCHF
PSPM	25p: 83.3 kCHF	26p: 87.8 kCHF
Instrumentation	10 kCHF	10 kCHF
SF housing	7 kCHF	10 kCHF
PSPM housing	7 kCHF	16 kCHF
Vacuum flange and shield	0	15 kCHF
Light shield	0	3 kCHF
Manpower	25 kCHF	15 kCHF
Position Sensitive Circuit	340ch: 34 kCHF	384ch: 38.4 kCHF
Trigger Logic Circuit	1×170ch 20 kCHF	1×384ch: 48 kCHF
TDC (3377)	11: 88 kCHF	12: 96 kCHF
HV power supply	24ch: 2.8 kCHF	2×24ch: 5.7 kCHF
Crate	2p: 12 kCHF	2p: 12 kCHF
Cables	20 kCHF	10 kCHF
Others	10 kCHF	10 kCHF
Total sum	345.1 kCHF	387.9 kCHF

Micro Drift Chambers

TDC "D408" (30 units)	40.8 kCHF
Driver "N403" (3 units)	3 kCHF
Controller "N404" (1 unit)	3 kCHF
Controller "K427" (1 unit)	3 kCHF
Total sum	49.8 kCHF

Freon 114 detectors upgrade

Mechanics (2 counters)	20 kCHF	Incl. Modification of mechanics of present Cherenkov counters
Mirrors (4)	0	Existing from present Cherenkov
Photomultiplier (4) (Hamamatsu R1587)	15.5 kCHF	w. standard UV-glass window incl. HV divider
Gas distribution system	3 kCHF	
Front-end electronics	12 kCHF	6 channels of FERA ADC 2 channels of Discriminators 1 Linear FIFO module
HV power supply (4 chan)	0	Existing from present Cherenkov
Cabling	1 kCHF	
Total sum	51.5 kCHF	

Silica aerogel detector*

Mechanics (1 module)	4 kCHF	Incl. Support for module and PM
Silica aerogel (28 tiles)	$\sim$ 2.8 kCHF	dim. $150 \times 100 \times 25$
Photomultiplier (2) (Hamamatsu R1587)	7.8 kCHF	w. standard UV-glass window Incl. HV divider
Front-end electronics	0	Existing from Freon 114 detectors
HV power supply (2 chan)	0	Existing from present Cherenkov
Cabling	1 kCHF	
Total sum	15.6 kCHF	

* Based on estimated price for the Silica aerogel.
No estimate for the manpower included.

8.2 Time scale for the $A_{\pi K}$ experiment

The following strategy can be foreseen for the experiment:

2002 Complete the data taking started in 2001 for the $A_{2\pi}$ lifetime measurement with the 10% design precision with the present setup geometry. Installation of the modified and tested Cherenkov counters, the aerogel counters and the third scintillating fibre plane. The setup tuning for observation of $A_{\pi K}$.

2003 Installation of the fourth plane SFD and one of the proposed precise coordinate detectors upstream the magnet. Data taking for the $A_{\pi K}$ observation.

2004–2005 Modification of the setup geometry. Measurement of $A_{\pi K}$ lifetime and refinement of the $A_{2\pi}$ lifetime to a precision better than 10%

Acknowledgements

We are grateful to J. Gasser and A. Rusetsky (Bern University) for their invaluable help in writing the theoretical part of our addendum. For many interesting and stimulating discussions about status and future of the underlying theory (especially pion-kaon scattering) we also thank P. Büttiker, G. Colangelo, W. Jaus, M. Knecht, H. Leutwyler, U. Meißner, G. Rasche, H. Sazdjian and J. Stern. Furthermore we acknowledge the kind and competent support in all technical aspects of DIRAC by the CERN PS division.

We thank the CERN Research Director C. Detraz and the EP Division Leader G. Goggi for their encouragements and support to the DIRAC experiment.

Appendix A

Modification procedure

This section illustrates the procedure for modifying the present setup. It is described in details to show that it may be achieved with minor effort and tooling.

1. Secondary beam channel, collimator and iron shielding, vacuum pipe and vacuum chamber

The wide vacuum pipe housing the proton beam line, and the secondary particles channel:

— attaching the pipe ends (whose axes coincide with the proton beam) to two temporary supports;

— removing the movable parts of the main support and rotating the wide pipe, with respect to the proton beam axis, by 14.5°;

— fixing movable parts of the main support in a new position and removing temporary supports;

— drilling new holes, at an angle of 14.5° with respect to the existing ones, in one of the flanges of the bellows connecting the target station to the wide pipe, and assembling the wide pipe with the target station and the proton beam line.

The collimator and the iron shielding:

— opening a small part of the shielding roof;

— removing, with the crane, one fourth of the iron wall;

— installing a wedge-like spacer (the angle of the wedge is 1.5°) close to the collimator where part of the wall is removed;

— putting the dismounted pieces of the wall in the new position close to the spacer;

— removing the spacer, and placing the collimator together with the existing wedges (5.7°) next to the reinstalled part of the wall;

— dismounting and putting the next one fourth of the wall close to the collimator.

The vacuum pipe between the collimator and flat vacuum chamber:

— replacing the existing rails of the vacuum pipe with more rigid ones;

— sliding the pipe on the rails in the new position;

— assembling the pipe and the collimator.

The flat vacuum chamber:

— moving the chamber downstream by 78 mm;

— displacing the chamber by 10 mm to the left size of the coils;

— rotating the chamber, with respect to known axis, by 4°.

These procedures can be accomplished without crane.

Insertion of a new part between the wide pipe and the flat chamber:

— in order to connect the wide pipe with the flat chamber in the new position, it will be necessary to put a new insertion.

2. Detectors upstream of the magnet (MSGC, SFD and IH)

MSGC and SFD: these detectors are attached to a common support which is placed on a platform. Thus, it will be easy to move them in the new position.

IH: this detector has a big support attached to the floor. If a new SFD were installed the IH would be removed.

3. Detectors downstream of the magnet (DC, VH, HH, C, PSh and Mu with iron absorbers)

DC, VH and HH: all these detectors are placed on a common platform. Therefore, it will be sufficient to displace the platform, parallel to the secondary beam axis, by 120 mm and to rotate it by 4° with respect to the magnet centre. This procedure can be done using a crane (after opening part of the roof) and some ad hoc means. Nevertheless, it would be possible to use only the latter (small fork lifts, jacks and screws).

C: for these detectors only a rotation of 4° will be necessary with respect to the magnet center. Before this operation, it will be necessary to attach additional jacks to the counters. In this way, using small fork lifts, it will be possible to move the counters in order to have the new jacks placed on the existing supports.

PSh, Mu and iron absorbers: The PSh and Mu counters will be just translated in their own planes, while the iron absorbers will not be moved. It will be necessary to add some iron bricks on the left sides of both absorbers.

Appendix B

Micro Drift Chambers as a DIRAC upstream coordinate detector

Drift chambers play a very important role in the present DIRAC experiment. They provide track reconstruction with a high efficiency and with high spatial resolution. Rigid mechanical design, rather simple production technology, nice features of read-out electronics make the drift chamber technique also attractive for particle tracking between target and magnet.

The distinctive property of "atomic pairs" is the passage of two charged particles at a rather small relative distance while detected upstream of the magnet. Therefore, upstream coordinate detectors have to detect tracks with high spatial resolution and at the same time to resolve nearby tracks. In the following we propose a design of Micro Drift Chamber, which combines high space and time characteristics with relatively high double track resolution.

Let us consider how particles are detected in a drift chamber cell. In case of one particle, primary ionisation electrons drift to an anode wire and initiate the avalanche process. This avalanche occupies part of the anode wire ("dead zone") and inhibits the detection of another particle close-by in space. An additional limitation arises from read-out electronics. Even if two particles are detected on the anode wire itself, a later signal may not be accepted by the multi-hit TDC due to a finite double-hit resolution. These limitations are fatal only in case of a single plane chamber. An additional plane, shifted by half a cell width, eliminates not only a left-right ambiguity, but also the double track resolution problem (fig. B.1). If two tracks cross one cell, one particle is detected by the first plane and the other by the second plane.

In the same figure a schematic layout of a double plane chamber is presented. Each plane consists of 32 cells. The cell size is 3×2 mm^2, and the sensitive area is 94.5×94 mm^2.

The chamber will be operated in a high current avalanche mode, most probably with the gas mixture $\mathrm{Ar}(0.33) + i\mathrm{C_4H_{10}}(0.66) + \mathrm{H_2O}(0.01)$. This will permit to use the present drift chamber read-out electronics, which has demonstrated perfect operating features.

Drift parameters, time and space resolution of the chamber have been investigated with help of the GARFIELD simulation package, and the counting rate capability has been estimated from our "dead zone" measurement.

Drift times (T_{dr}) and spreads of arrival time (σ_t) as a function of drift distance are shown in fig. B.2. The drift time T_{dr} exhibits rather linear dependence, what is very

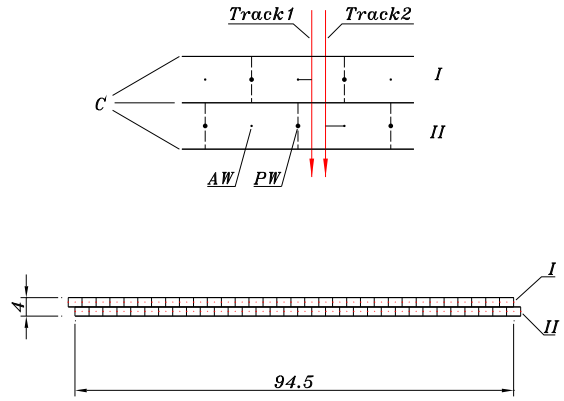

Figure B.1: Schematic layout of a double-plane drift chamber: AW — anode wires, 50 μm in diameter; PW — potential wires, 100 μm in diameter; C — cathode, Mylar foil, 20 μm thick. Sizes are measured in mm.

convenient for track reconstruction procedures. The maximum drift time is 26 ns. The σ_t value never exceeds 0.5 ns, thus the spatial resolution is better then 30 μm.

The double track resolution of the double plane chamber is illustrated in fig. B.3. The histograms correspond to two tracks separated by 100 μm in space. The left histogram corresponds to tracks detected by the first plane, and the right one to tracks detected by the second plane. The TDC bin width, of 0.5 ns, has been taken into account.

We plan to install the micro drift coordinate detector, consisting of three double plane chambers, along each coordinate (X and Y) in the region, where the present upstream detectors are located. A full track reconstruction near the target should be achievable. The present drift chamber readout electronics will be utilised.

The most important features of the detector are:

- spatial accuracy $\sigma < 30$ μm,
- double track resolution < 200 μm,
- one plane efficiency at beam intensity $I = 2 \cdot 10^{11}$ protons per spill, due to the "dead zone" $> 98\%$,
- low multiple scattering: total detector thickness $< 5 \cdot 10^{-3}$ X_0,
- time resolution $\sigma < 1$ ns,
- low track multiplicity < 3 tracks,
- small readout time < 3 μs.

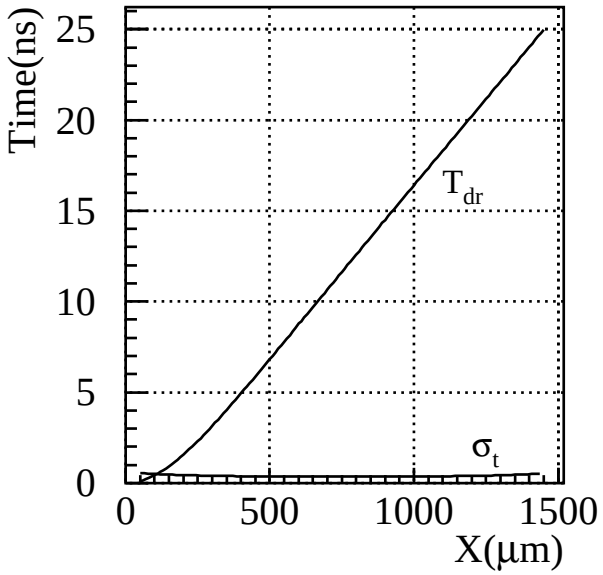

Figure B.2: *Time features of the drift chamber simulated with help of the GARFIELD package. Gas mixture is* $\mathrm{Ar}(0.33) + i\mathrm{C_4H_{10}}(0.66) + \mathrm{H_2O}(0.01)$.

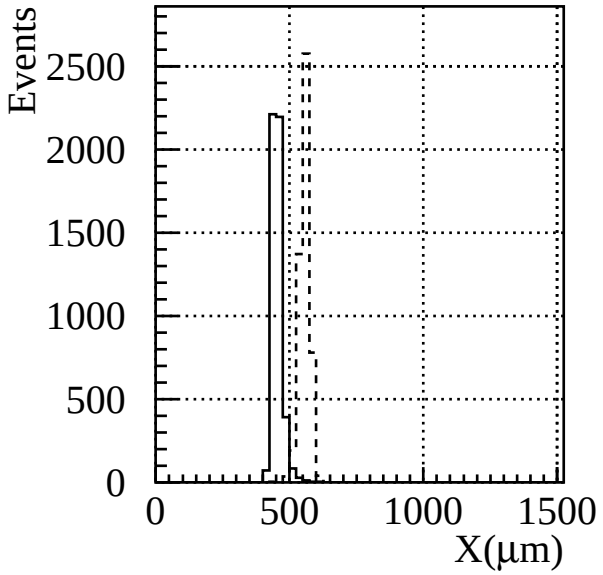

Figure B.3: *The double track resolution of the double-plane drift chamber. The solid histogram corresponds to track position* 450 μm *and the dashed one to* 550 μm *with respect to the anode wire.*

Main advantages:

- rather simple and cheap production technology,
- inexpensive readout electronics, similar to the read-out electronics used in present Drift Chambers,
- our long and successive experience in drift chamber technique,
- detector production could be performed by the collaboration,
- total cost of the system, including spare units, will be less than 50 kCHF.

Bibliography

[ADEV95] B. Adeva, *et al.*, CERN/SPSLC 95–1, SPSLC/P 284, Geneva 1995.

[AFAN91] L. G. Afanasyev, JINR E2-91-578, Dubna, 1991;
JINR B1-2-91-572, Dubna, 1991.

[AFAN93] L. G. Afanasyev et al., Phys. Lett. **308B** (1993) 200.

[AFAN93A] L. G. Afanasyev, A. V. Tarasov, JINR E4-93-293, Dubna, 1993.

[AFAN94] L. G. Afanasyev et al., Phys. Lett. **338B** (1994) 478.

[AFAN96] L. G. Afanasyev and A. V. Tarasov, Yad.Fiz. **59** (1996) 2212; Phys. At. Nucl. **59** (1996) 2130.

[AFAN97] L. G. Afanasyev, O. Voskresenskaya and V. Yazkov, JINR preprint, P1-97-306, Dubna, 1997.

[AFAN97A] L. G. Afanasyev, "Observation of $\pi^+\pi^-$ atom", PhD thesis, JINR, Dubna, 1997.

[AFAN99] L. G. Afanasyev, A. V. Tarasov and O. Voskresenskaya, J. Phys. **G25** (1999) B7-B10.

[AFAN99A] L. G. Afanasyev and O. Voskresenskaya, Phys. Lett. **B453** (1999) 302.

[AFAN00] L. G. Afanasyev and S. Santamarina, DIRAC note 00-04

[AGUI73] M.Aguilar-Benitez *et al.*, Phys. Rev. Lett. **30** (1973) 672.

[AMIR99] I. Amirkhanov *et al.*, Phys. Lett. **452** (1999) 155.

[ANTI71] P. Antich *et al.*, Nucl. Phys. **B29** (1971) 305.

[AOKI99] S. Aoki *et al.*, hep-lat/9911025.

[BACH99] N. Bacchetta *et al.*, Nucl. Instr. and Meth. **A426** (1999) 16.

[BAKE75] S. L. Baker *et al.*, Nucl. Phys. **B99** (1975) 211.

[BAKE99] N. van Bakel *et al.*, Snowmass 1999, "Electronics for LHC experiments", 167.

[BAKK70] A. M. Bakker *et al.*, Nucl. Phys. **B24** (1970) 211.

[BALD76] R. Baldi *et al.*, Phys.Letters **63B** (1976) 344.

[BALD78] R. Baldi *et al.*, Nucl. Phys. **B134** (1978) 365.

[BAUE99] C. Bauer *et al.*, Snowmass 1999, "Electronics for LHC experiments", 508.

[BAYE69] V. N. Bayer and V. S. Fadin, Zh. Eksp. Teor. Fiz. **57** (1969) 225; Sov. Phys. JETP **30** (1970) 120.

[BERN91] V. Bernard, N. Kaiser and U. Meissner, Phys. Rev. **D43** (1991) 2757;
V. Bernard, N. Kaiser and U. Meissner, Nucl. Phys. **B357** (1991) 129.

[BIJN96] J. Bijnens *et al.*, Phys. Lett. **B374** (1996) 210.

[BIJN97] J. Bijnens *et al.*, Nucl. Phys. **B508** (1997) 263; (hep-ph/9707291).

[BILE69] S. M. Bilenky *et al.*, Yad. Fiz. **10** (1969) 812; Sov. J. Nucl. Phys. **10** (1969) 469.

[BING72] H. H. Bingham *et al.*, Nucl. Phys. **B41** (1972) 1.

[BRAG99] M. Bragadireanu *et al.*, Nucl. Instr. Meth. **A426** (1999) 254.

[BRAN77] G. W. Brandenburg *et al.*, not published, (1977).

[BRES99] A. Bressan *et al.*, Nucl. Instr. and Meth. **A425** (1999) 254

[CERN00] CERN/LHCC 2000-016 CMS TDR 5 Addendum 1, 21 Feb. 2000.

[CHLI75] P. V. Chliapnikov *et al.*, Phys.Letters **55B** (1975) 237.

[CHO70] Y. Cho *et al.*, Phys Lett. **32B** (1970) 409.

[CHPT] For recent reviews on CHPT see:
H. Leutwyler, [LEUT93];
U. G. Meißner, Rep. Prog. Phys. **56** (1993) 903;
A. Pich, Lectures given at the V Mexican School of Particles and Fields, Guanajuato, México, December 1992,
preprint CERN-Th.6978/93 (hep-ph/9308351);
G. Ecker, Chiral perturbation theory, in: Quantitative Particle Physics: Cargèse 1992, Eds. M. Lévy et al., Plenum Publ. Co. (New York, 1993);
J. F. Donoghue, E. Golowich. and B. R. Holstein, "Dynamics of the Standard Model" (1992), Cambridge University Press, Cambridge.

[COLA00] G. Colangelo *et al.*, hep-ph/0007112.

[DEBA69] W. De Baere *et al.*, Nucl. Phys. **B14** (1969) 425.

[DENI87] K. G. Denisenko and S. Mrowczynsky, Phys.Rev. **D36** (1987) 1529.

[DESC00] S. Descotes and J. Stern, hep-ph/0007082.

[DUNW77] W. M. Dunwoodie *et al.*, not published, (1977).

[EFIM86] G. V. Efimov, M. A. Ivanov and V. E. Lyubovitskij, Yad. Fiz. **44** (1986) 460; Sov. J. Nucl. Phys. **44** (1986) 296.

[EFIM87] G. V. Efimov, M. A. Ivanov and V. E. Lyubovitskij, Pis'ma Zh. Exp. Teor. Fiz. **45** (1987) 526.

[EICH72] T. Eichten *et al.*, Nucl. Phys. **B44** (1972) 333.

[ESTA78] P. Estabrooks *et al.*, Preprint SLAC-PUB-1886 and Nucl. Phys. **B133** (1978) 490.

[FIRE72] A. Firestone *et al.*, Phys.Rev. **D5** (1972) 2188.

[FOX74] G. C. Fox and M. L. Griss, Nucl. Phys. **B80** (1974) 403.

[FUCH91] M. H. Fuchs, H. Sazdjian and J. Stern, Phys. Lett. **B269** (1991) 183.

[FUKU95] M. Fukugita *et al.*, Phys. Rev. **D52** (1995) 3003.

[GALL99] A. Gall, J. Gasser, V. E. Lyubovitskij and A. Rusetsky, Phys. Lett. **B462** (1999) 335.

[GARW71] E. L. Garwin and A. Roder, Nucl. Instr. and Meth. **93** (1971) 593.

[GASS83] J. Gasser and H. Leutwyler, Phys. Lett. **B125** (1983) 327.

[GASS99] J. Gasser, V. E. Lyubovitskij and A. G. Rusetsky, Phys. Lett. **B471** (1999) 244.

[GASS00] J. Gasser and A. G. Rusetsky private comunication.

[GASH98] A. Gashi *et al.*, Nucl. Phys. **A628** (1998) 101.

[GELL68] M. Gell-Mann, R. J. Oakes and B.'Renner, Phys. Rev. **175** (1968) 2195.

[GLAS68] S. Glashow and S. Weinberg, Phys. Rev. Lett. **20** (1968) 224.

[GOME97] F. Gómez *et al.*, Nucl. Instr. and Meth. **A384** (1997) 351.

[GORC99] O. E. Gorchakov, A. V. Kuptsov, L. L. Nemenov, D. Y. Riabkov, preprint, JINR E1-99-134, Dubna 1999.

[GORC00] O. E. Gorchakov *et al.*, Yad. Fiz. **69** (2000) 1015.

[GRAE77] H. Graessler *et al.*, Nucl. Phys. **B125** (1977) 189.

[GRIS82] V. G. Grishin "Inclusive processes in hadron interaction at high energy", Energoizdat, Moscow 1982, 131.

[HALA99] Z. Halabuka *et al.*, Nucl. Phys. **554** (1999) 86.

[HART94] E. Hartouni *et al.*, Phys. Rev. Lett. **72** (1994) 1322.

[HEIN76] J. Heintze *et al.*, Nucl. Instr. and Meth. **138** (1976) 641.

[HORI93] R. Horisberger and D. Pitzl, Nucl. Instr. and Meth. **A326** (1993) 92.

[HUBB75] J. H. Hubbel *et al.*, J. Phys. Chem. Ref. Data **4** (1975) 71.

[HUBB79] J. H. Hubbel, I. Overbo, J. Phys. Chem. Ref. Data **8** (1979) 9.

[IVAN99] M. A. Ivanov, V. E. Lyubovitskij, E. Z. Lipartia and A. G. Rusetsky, Phys. Rev. **D58** (1998) 0094024.

[IVAN99A] D. Yu. Ivanov and L. Szymanowski, Eur.Phys. J.**A5** (1999) 117.

[JALL99] H. Jallouli and H. Sazdjian, Phys. Rev. **D58** (1998) 014011; 099901(E).

[JOHA78] N. Johannesson and G. Nilsson, Nuovo Cimento **43A** (1978) 376.

[JONE99] L. L. Jones *et al.*, Snowmass 1999, "Electronics for LHC experiments", 162.

[JONG73] B. Jongejans *et al.*, Nucl. Phys. **B67** (1973) 381.

[KARA80] A. Karabarbouris and G. Shaw, Journal of Phys. **G6** (1980) 583.

[KARI86] A. Karimhodjaev and R. N. Faustov, JINR, P2-86-142, Dubna, 1986.

[KIRS71] A. R. Kirschbaum *et al.*, Phys.Rev. **D4** (1971) 3254.

[KNEC93] M. Knecht 28th Rencontre de Moriond : QCD and High-energy Hadronic Interactions - Particle Physics Meetings, Les Arcs, France, 20 - 27 Mar 1993 / Ed. by J Tran Thanh Van. - Ed. Frontieres, Gif-sur-Yvette, (1993) 187.

[KNEC93A] M. Knecht *et al.*, Phys. Lett. **B413** (1993) 229.

[KNEC95] M. Knecht *et al.*, Nucl. Phys. **B457** (1995) 513.

[LANG77] C. B. Lang, Nuovo Cimento **41A** (1977) 73.

[LANG78] C. B. Lang, Fortschrinder für Physik, **26** (1978) 509.

[LAUS75] P. Lauscher *et al.*, Nucl. Phys. **B86** (1975) 189.

[LEDN82] R. Lednicky and V. L. Lyuboshits, Yad. Fiz. **35** (1982) 1316; Sov. J. Nucl. Phys. **35** (1982) 770.

[LEUT93] H. Leutwyler, Proc. XXVI Int. Conf. on High Energy Physics, Dallas, 1992, edited by J. R. Sanford, IAP Conf. Proc. N.272 (AIP New York 1993) 185.

[LEUT94] H. Leutwyler, Ann. Phys. **235** (1994) 165; (hep-ph/9311274).

[LING73] D. Linglin *et al.*, Nucl. Phys **B55** (1973) 408; Nucl. Phys. **B57** (1973) 64.

[LUBO97] V. E. Lyubovitskij, E. Z. Lipartia and A. G. Rusetsky, Pis'ma Zh. Exp. Teor. Fiz **66** (1997) 747.

[MART78] A. D. Martin *et al.*, Nucl. Phys. **B134** (1978) 392.

[MATI74] M. J. Matison *et al.*, Phys. Rev. **D9** (1974) 1872.

[MERC71] R. Mercer *et al.*, Nucl. Phys. **B32** (1971) 381.

[MOLI47] G. Moliere, Z. Naturforsch. **2A** (1947) 3.

[MOOR95] U. Moor, G. Rasche and W. S. Woolcock, Nucl. Phys. **A587** (1995) 747.

[MROW87] S. Mrowczynski, Phys. Rev. **D36** (1987) 1520.

[NEME85] L. L. Nemenov, Yad. Fiz **41** (1985) 980; Sov. J. Nucl. Phys. **41** (1985) 629.

[NILS87] B. Nilsson-Almquist, E. Stenlund, Com. Phys. Comm. **43** (1987) 387.

[OLSH00] V. G. Olshevsky, S. V. Trusov, JINR E10-2000-150, Dubna, 2000.

[OLSH00A] V. G. Olshevsky, S. V. Trusov, DIRAC internal note 00-06.

[ROES99] A. Roessl, Nucl. Phys. **B555** (1999) 507; (hep-ph/9904230).

[SAKH48] A. D. Sakharov, Zh. Eksp. Teor. Fiz. **18** (1948) 631.

[SALV87] F. Salvat *et al.*, Phys. Rev. **A36** (1987) 467.

[SAZD00] H. Sazdjian, hep-ph/0004226.

[SJOS87] T. Sjöstrand, M. Bengtsson, Com. Phys. Comm. **43** (1987) 367.

[SPIR77] M. Spiro *et al.*, Saclay preprint DPhPE 77/05 (1977).

[STER93] J. Stern, H.Sazjian and N.H. Fuchs, Phys. Rev. **D47** (1993) 3814.

[SUMI99] T. Sumiyoshi *et al.*, Nucl. Instr. and Meth. **A433** (1999) 385.

[TARA91] A. V. Tarasov and I. U. Christova, JINR P2-91-10, Dubna, 1991.

[TRIP68] T. G. Trippe, Phys. Lett. **28B** (1968) 143.

[URIB94] J. Uribe *et al.*, Phys. Rev. **D49** (1994) 4373.

[WEIN66] S. Weinberg, Phys. Rev. Lett. **17** (1966) 616.

[WEIN68] S. Weinberg, Phys. Rev. **166** (1968) 1568.

[WEIN79] S. Weinberg, Physica **96A** (1979) 327.

[YUTA71] H. Yuta *et al.*, Phys. Rev. Lett. **26** (1971) 1502.